Session 13

Multi-phase

S13-A2 Hugo D. Bernardino Amaro — Effect of hydrodynamic drag on uniformly coated spherical carrier particles

S13-A3 Hani Elmestikawy — 2nd International Symposium on AI and Fluid Mechanics Data-driven hydrodynamic force correlations for Euler-Lagrange simulations of particle-laden flows

S13-A4 Hendrik Hessenkemper — Deep Learning Models for 3D Lagrangian tracking in disperse 3-phase flows

S13-A5 Jiayang Xu — Multi-Fidelity Heteroscedastic Gaussian Processes for Cavitation Wall Load Prediction

S13-A8 Bruno Delhom — Development of a multi-species real fluid modeling

S13-P1 Vinicius G. Poletto — CFD-DEM modeling of particle clustering and deposition combining growth and adhesion

S13-P6 Connor Nolan — Machine Learning-Based Prediction of Non-Spherical Particle Agglomeration

S13-P7 Zikai Zhang — Full-Field Reconstruction of Droplet Impact via Multi-Fidelity Physics-Informed Neural Networks

S13-P10 Lee Mortimer — Prediction of Turbophoretic Particle Transport in Wall-Bounded Turbulent Flows Using Long Short-Term Memory Neural Networks

S13-P11 Xuan-Qi Liu — Resilient groundwater flow modeling in heterogeneous porous media using mixed-form PINNs and transfer learning

Effect of hydrodynamic drag on uniformly coated spherical carrier particles

Hugo D. Bernardino Amaro[a,*], Manuel A. Taborda[a], Berend van Wachem[a]

[a]*Chair of Mechanical Process Engineering, Otto-von-Guericke-Universität, Magdeburg, 39106, Germany*

Abstract

In recent years, computational techniques have significantly enhanced the understanding of the mechanisms governing drug aerosolization and administration in dry powder inhalers. Nevertheless, they remain fundamentally limited by the accuracy of the drag, lift, and torque correlations applied to discrete particle clusters. Commonly used empirical correlations, such as the Schiller-Naumann equation, assume smooth spherical geometries. However, carrier-fines agglomerates exhibit significant deviations in aerodynamic behavior, analogous to the effects induced by surface roughness. To quantify this effect, this work investigates the hydrodynamic drag on spherical carrier particles uniformly coated with fines, utilizing particle-resolved direct numerical simulations to develop a regime-dependent predictive model for the relative drag enhancement experienced by these agglomerates. The flow around carrier-fines agglomerates is resolved using the immersed boundary method. The agglomerate geometries are defined by a fixed fine-to-carrier diameter ratio. These configurations are parameterized by the surface coverage ratio, defined as the ratio of the carrier surface area covered by fine particles to the total surface area of the carrier. Simulations are conducted across discrete ranges of surface coverages and flow regimes, spanning late-creeping flow to the early inertial transition.

Initial analysis demonstrates that approximating these agglomerate configurations as a single, smooth encapsulating sphere leads to a non-negligible overestimation of the hydrodynamic drag. We evaluate the relative drag enhancement, which quantifies the relative increase in drag relative to a smooth, isolated carrier particle under identical flow conditions. Results show a strictly positive relative drag enhancement for all considered configurations. At low surface coverages, the relative enhancement in drag exhibits a linear increase with surface coverage. However, as surface coverage grows, a saturation mechanism emerges, where inter-particle wake shielding happens between the fine particles. By analyzing the rate of increase in relative drag enhancement, we describe this mechanism by proposing a Langmuir-type saturation model, parameterized by a characteristic saturation threshold and an asymptotic maximum drag ceiling. By normalizing the relative drag enhancement against its asymptotic plateau and the coverage against the saturation threshold, the data across all investigated regimes collapses onto a single universal curve.

Finally, we establish that the drag behavior of carrier-fines agglomerates is governed by two competing mechanisms, the absolute magnitude of individual particle drag and the onset of wake-induced saturation. By parameterizing these mechanisms as empirical functions of the Reynolds number, we propose an extension to the Schiller-Naumann correlation. This model accurately predicts the drag on coated carrier particles when compared to the results obtained from the particle-resolved simulations, providing a closure model for the estimation of drag for carrier-fines agglomerates, which can be used in Euler-Lagrange simulations.

Keywords: Enhanced drag modeling, Non-spherical particles, Langmuir-type model, Dry powder inhalers

*Corresponding author

Email address: hugo.bernardino@ovgu.de (Hugo D. Bernardino Amaro)

Data-driven hydrodynamic force correlations for Euler-Lagrange simulations of particle-laden flows

Hani Elmestikawy[1], Akshay Chandran[1], Bruno Blais[2], Max Hausmann[1], and Berend van Wachem[1]

1: Chair of Mechanical Process Engineering, Otto-von-Guericke-Universität, Magdeburg, Germany
2: Chemical engineering High-performance Analysis, Optimization and Simulation (CHAOS) laboratory, Department of Chemical Engineering, Polytechnique Montréal, Canada

Abstract

Accurate prediction of the hydrodynamic forces on particles is central to the fidelity of Euler-Lagrange (EL) simulations of particle-laden flows. Traditional EL methods typically rely on determining the hydrodynamic forces (*i.e.,* drag, lift, etc.) at the positions of the individual particles from the interpolated *undisturbed* fluid velocity field and its gradients. Existing hydrodynamic force models are semi-empirical because they rely on correlations derived from idealized conditions, such as uniform flows around isolated spheres, and therefore depend fundamentally on knowing the undisturbed velocity. However, recovering the undisturbed fluid velocity at the particle location, *i.e.,* the velocity the fluid would have in the absence of the particle, is both conceptually ambiguous and computationally prohibitive in general flow configurations, particularly in dense suspensions where overlapping flow disturbances from neighbouring particles render a clean separation intractable.

In this study, we propose a novel force prediction framework that circumvents the need for undisturbed velocity estimation by leveraging volume-filtered quantities available directly from EL simulations. Through extensive particle-resolved direct numerical simulations (PR-DNS) at finite Reynolds numbers, we employ state-of-the-art equivariant neural networks (ENNs) to determine the full hydrodynamic forces on each particle, with inputs consisting solely of volume-filtered fluid quantities, the local volume fraction and its gradients. By utilizing ENNs, rotational and translational symmetries are satisfied by the network architecture itself, rather than learning it, ensuring that the predicted hydrodynamic forces transform consistently with the non-scalar input features. Additionally, using a symbolic fit, we propose an equation for the drag force on individual particles, that inherently respects symmetries in the particle microstructure. The resulting model is shown to recover known drag laws in the appropriate asymptotic limits and exhibits good agreement with analytical and high-fidelity numerical benchmarks for single particle cases, and, compared to existing correlations, an improved agreement for the drag force on particles in particle assemblies. The proposed framework significantly enhances the accuracy of hydrodynamic force predictions for both isolated particles and dense suspensions, without incurring the prohibitive computational costs associated with reconstructing undisturbed flow fields. This advancement lays the foundation for robust, scalable, and high-fidelity EL simulations of complex particulate flows across a wide range of industrial and environmental applications.

Deep Learning Models for 3D Lagrangian tracking in disperse 3-phase flows

Hendrik Hessenkemper[1,*], Guangyuan Huang[1], Lantian Wang[1],Tian Ma[1]
[1] *Institute of Fluid Dynamics, Helmholtz-Zentrum Dresden – Rossendorf, Dresden 01328, Germany*
*Corresponding author(s): h.hessenkemper@hzdr.de (H. Hessenkemper)

Abstract

The detection and tracking of dispersed phases in multiphase flows is a quite a challenge due to the strong image occlusions by the different phases, severe object overlaps and potential varying object shapes. We devote our recent developments on one of such cases, namely 3-phase bubbly flows with millimetric, deformable bubbles together with inertial glass beads, in which we not only want to track these two dispersed phases, but also seeded tracer particles in the surrounding liquid bulk. To detect and distinguish the different objects, we present two different deep learning models, namely an adapted Detection Transformer for the comparably large and irregular shaped gas bubbles, and a Particle Discriminator UNet to distinguish between glass beads and tracer particles. To demonstrate the capabilities of our models, we use synthetic as well as experimental shadowgraphy, multi-view camera recordings and utilize a simultaneous 3D Lagrangian tracking of all three object types using the Shake-the-Box approach [1] for the tracers and glass beads, together with our own developed Langragian bubble tracker for deformable bubbles [2].

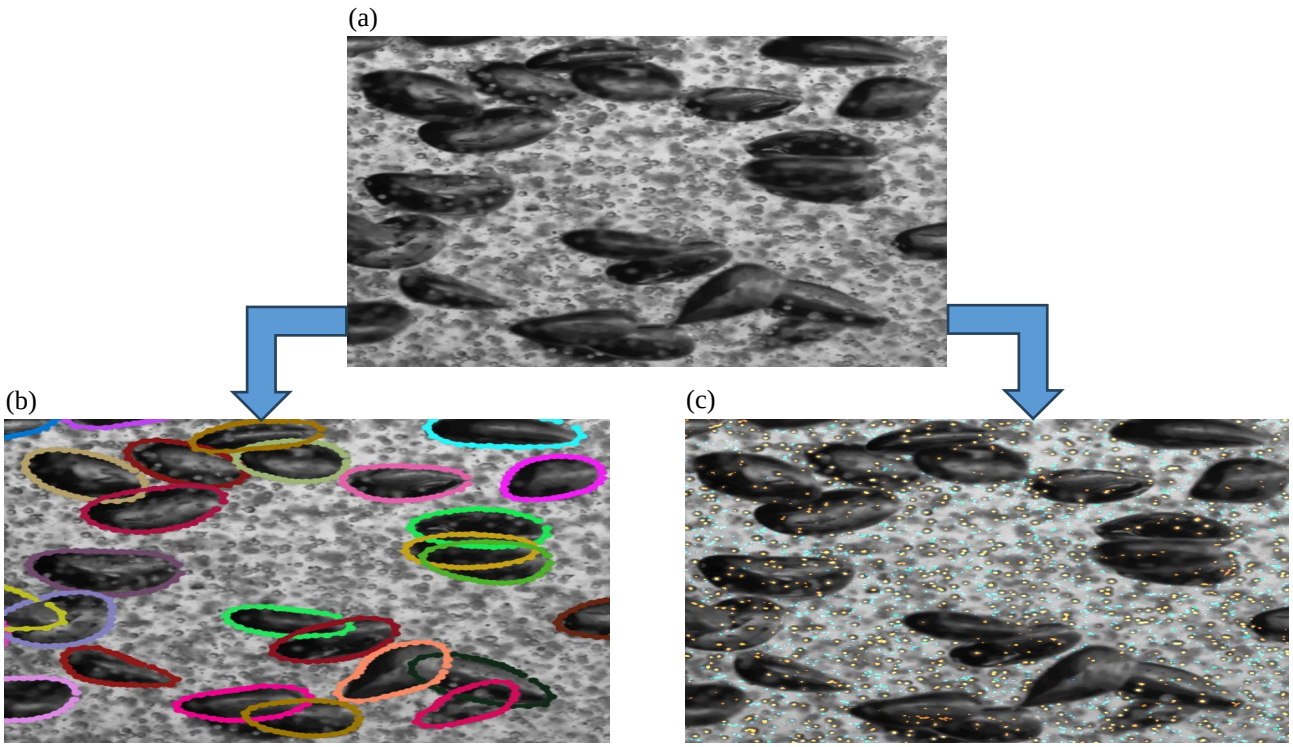

Figure 1: Visualization of the different model predictions. (a) Experimental image containing deformable bubbles (large, dark objects), glass beads (smaller, circular objects) and tracer particles (tiny, black dots). (b) Bubble outlines detected by the Detection Transformer, where different colors represent different bubbles. (c) Heatmap of different particle centroids generated by the Particle Discriminator UNet. Yellow heatmap refers to glass beads and blue heatmap refers to tracer particles. All images cropped w.r.t. original image for better visualization.

References

[1] Schanz, D., Gesemann, S., Schröder, A. (2016). Shake-The-Box: Lagrangian particle tracking at high particle image densities. Exp. Fluids 57, 70.

[2] Hessenkemper, H., Wang, L., Lucas, D., Tan, S., Ni, R., Ma, T. (2024). 3D detection and tracking of deformable bubbles in swarms with the aid of deep learning models. Int. J. Multiphase Flow 179, 104932.

Keywords: Lagrangian Particle Tracking, Bubbly Flows, Computer Vision

Multi-Fidelity Heteroscedastic Gaussian Processes for Cavitation Wall Load Prediction

[1]Jiayang Xu*; [1]Josef Winter; [1] Steffen Schmidt; [1,2] Nikolaus A. Adams

[1]*Chair of Aerodynamics and Fluid Mechanics, School of Engineering and Design, Technical University Munich, Boltzmannstr.15, Garching 85748, Germany*

[2]*Munich Institute of Integrated Materials, Energy and Process Engineering, Technical University Munich, Lichtenbergstr.4a, Garching, 85748, Germany*

[*]*jiayang.xu@tum.de*

Abstract

Modeling the resolved dynamics of cavitation to accurately predict wall loads or estimate erosion presents a significant computational challenge. The prohibitive cost of high-fidelity Computational Fluid Dynamics renders parametric studies across unbounded configuration spaces impractical. To overcome these limitations, we propose a Multi-Fidelity Variational Heteroscedastic Gaussian Process (MFVHGP) strategy. This approach is driven by hierarchical simulation data comprising extensive coarse-grid bubble-cloud simulations and a sparse set of highly resolved benchmarks. A nonlinear autoregressive process with augmented data is used to pass information between fidelity levels, and uncertainties are propagated across these levels. Variational GPs and a Linear Model of Coregionalization are used at each fidelity level to model the heteroscedastic uncertainty in the data, given that the physics of bubble collapse is inherently chaotic, exhibiting extreme variance during the collapse stage. For a bubble cluster, the configuration and geometry of the cluster, as well as its stand-off distance, dominate the wall impact; therefore, selected geometrical parameters and the stand-off distance are used as model inputs, and the maximum wall pressure is predicted. The results demonstrate that the MFVHGP effectively learns inter-mesh correlations and reconstructs the high-fidelity response using significantly fewer high-fidelity samples than single-fidelity Gaussian processes. By augmenting scarce high-fidelity data with inexpensive low-fidelity simulations, the framework improves predictive accuracy and captures key physical transitions. Future work aims to extend the model to different fidelity levels beyond resolution, and across different data sources to further improve scalability.

Keywords: Gaussian Processes, Multi-Fidelity Modeling, Cavitation Dynamics, Machine Learning, Uncertainty Quantification, Multiphase Flow

Development of a multi-species real fluid modelling approach using an innovative machine learning method, application to MASCOT.

[1]Bruno Delhom*; [1]Chaouki Habchi ; [1]Olivier Colin ; [1]Julien Bohbot;

[1]*IFP Energies Nouvelles, Institut Carnot Transports Energies, 1 et 4 Avenue de Bois-Préau, 92852 Rueil-Malmaison, France*

[*] *Corresponding author: bruno.delhom@ifpen.fr*

Abstract

Two-phase flow configurations present many challenges for numerical modeling, requiring the development of Real Fluid Models (RFM) able to simulate flows in subcritical, transcritical or supercritical regimes. Such a RFM model has been recently developed at IFPEN. It uses a data-driven approach based on Vapor-Liquid Equilibrium (VLE) to handle the complex behavior of two-phase simulations. Specifically, a pre-calculated table was generated to store thermodynamic and transport property values for all possible mixtures within a defined range of temperature, pressure and mass fractions. This table was used during simulations but has limitations when the number of chemical species increases.

This article proposes an approach based on neural networks (NN) in line with what we presented last year at the first edition of the Ai-Fluids conference [1]. We will study a 3D MASCOT calculation (sectoral) of an H2/O2 flow that can be burned.

The kinetic scheme will involve around 30 species, which is innovative in an RFM approach. The methodology sed to couple the CONVERGE CFD code with neural networks will also be a new approach, with on-the-fly training of the neural networks.

[1] Delhom, Bruno & Habchi, Chaouki & Colin, Olivier & Bohbot, Julien. (2025). Development of a multi-species real fluid modelling approach using a machine learning method, application to combustion. 10.13140/RG.2.2.29896.23043.

.

Translated with DeepL.com (free version)**Keywords:** Subcritical, supercritical, transcritical flow, real fluid model, VLE, Neural network, ISAT.

Proceedings of the 2nd International Symposium on AI and Fluid Mechanics
Paper No [leave blank]

CFD-DEM modeling of particle clustering and deposition combining growth and adhesion

[1]Marina Elizabeth Mazuroski; [1]Thiago Machado Neubauer; [1]Vinicius Gustavo Poletto; [1]Fernando Cesar De Lai; [2]Bruno Barbosa Castro; [2]André Leibsohn Martins; [1]Silvio Luiz de Mello Junqueira*

[1]*Research Center for Rheology and Non-Newtonian Fluids, Federal University of Technology - Paraná, Curitiba 81280-340, Brazil;*

[2]*Petrobras - CENPES/PDIDP/EPOCOS/COMP*

Abstract

An Euler-Lagrange hybrid model to simulate liquid-solid two-phase flow with adhesion and particle growth is presented for the simulation of particle transport, agglomeration, and deposition. The numerical model is based on CFD-DEM with the inclusion of adhesion and particle resizing. The verification is by reproduction of literature results referring to particle settling, normal collision, oblique collision, and pile formation. The effects of adhesion and particle growth in liquid-solid flow considers an adhesive-weight ratio of 5.10^4 and particles growing from 20μm grow up to 40μm. It is possible to evaluate the individual and combined influence of adhesion and resizing, leading to distinct particle transport patterns. The influence of flow rate is also evaluated observing that there is a competitive effect between solid dispersion and diameter resizing that eventually leads to a favorable condition for bulk agglomerates build up that outbreak the pressure.

Keywords: CFD-DEM; particle growth; adhesion; particle clustering; scaling

Introduction

Inorganic scaling may occur in various equipment and industrial processes, sometimes subjected to high-pressure and high-temperature conditions [1, 2]. It refers to the unwanted formation and subsequent deposition of crystals formed by ions of inorganic salts. Examples of salts found in the fouling process are calcium carbonate and the sulfates of calcium, barium, and strontium, among others [3]. Being the driving force of the crystallization/scaling process, the substance's supersaturation occurs when a solute's solubility exceeds a limit value. Although a supersaturated system will not necessarily precipitate, supersaturation is essential for crystallization as some degree of disturbance may be necessary[4]. Nucleation, when forming the first crystals, may occur in the volume of the solution (homogeneous nucleation) or on surfaces and other particles (heterogeneous nucleation)[5]. Crystal growth and agglomeration happen by incorporating and assembling ions and crystals in other crystals [6]. Crystals can also adhere to surfaces, creating a solid layer that requires a certain amount of force to remove them [7]. The rate at which each mechanism ensues depends on supersaturation levels, surface properties, fluid flow conditions, heat and mass transfer rates, temperature, pressure, pH, and composition—mixture, among others, reflects the complex nature of the scale formation process. [8]

In the literature, the approach to modeling the scaling formation can be from a thermodynamic or kinetic point of view [9]. Thermodynamic models seek to predict saturation levels and precipitation potential based on the solution's equilibrium state. These models can contain information on solubility at different temperatures, pressures, and pH levels, accounting for the influence of certain substances in the mixture [10–13]. Kinetic models focus on nucleation, growth, and agglomeration rates under different conditions assuming an already supersaturated system [7, 14].

To model the particle-particle interactions in a dense particulate phase, the Discrete Element Method - DEM, initially described by [15], emerged as a tool to simulate the movement and forces in systems with millions of particles. The CFD-DEM [16] appears as a method based on the Euler-Lagrange approach, which couples the flow (continuous) with the solid (discrete) phase. The interparticle adhesive force using CFD-DEM has recently been applied to investigate the fouling process in a sliding sleeve valve (SSV) geometry employed in oil extraction procedures [17]. Ramirez et al. [18] employed CFD-DEM to test drag force correlations in gas-solid flow to investigate the effect of particle clustering in the catalyst deactivation in riser reactors. In a numerical and experimental work, Saparbayeva et al. [19] validated the coupled CFD-DEM approach with cohesion by modeling the oblique collision of an ice drop on an inclined ice surface immersed in decane.

Modeling the solid particle diameter variation, common in scaling formation or dissolution processes, has attracted the attention of some researchers. Dogonchi et al. [20] investigated the diameter reduction of solid particles due to

*Corresponding Author, Vinicius Gustavo Poletto vpoletto@utfpr.edu.br

dissolution in a non-Newtonian fluid. Using the Colocation Method, the authors modeled the particle diameter variation considering a linear function. Comparing mass transfer models for particle dissolution, Uzi et al. [21] applied to the CFD-DEM several user-defined functions to investigate the diameter reduction of NaCl particles in brine.

In light of the above, and considering the importance of particle adhesion and growth in processes such as fouling formation, it becomes evident that there is an opportunity to integrate these phenomena through a two-phase solid-liquid flow in a four-way approach. In this work, the CFD-DEM coupling available in the software ANSYS FLUENT is customized using UDFs (User Defined Functions) to represent the solid-fluid biphasic flow, including particle growth and adhesion, as depicted in the capillary duct of Figure 1. Accordingly, the spherical particles dispersed in the flow represent precipitated crystals of inorganic salt (such as barium sulfate or calcium carbonate, for example), that undergo a growth process. Simultaneously, the particles eventually interact with each other and with the capillary walls, thus resembling scale formation.

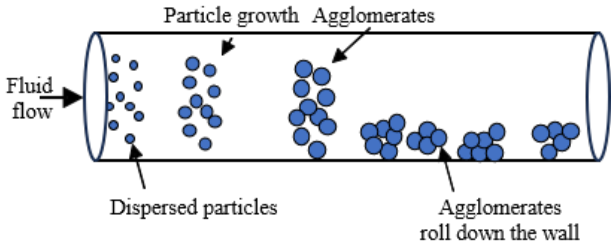

Figure 1: CFD-DEM applied to model dispersed solids transport, particle growth, and formation of agglomerates.

Problem geometry and formulation

Figure 2 displays the simulation domain represented by a tube with a cross-section of 0.5 mm diameter and 625 mm length, resulting in an aspect ratio of 1250. The fluid enters Region (1) with uniform velocity and develops along 80 *mm*. In Region (2), solids injection occurs in a surface placed at 100 *mm*, denoted by the red circle. In Region (3), the particulate flow leaves the capillary duct under uniform pressure conditions. The fluid and duct wall interaction occurs under no-slip conditions. In the sequence, particle-particle and particle-wall interactions due to collisional, frictional, and adhesive forces are presented. Particles continuously interact with the flow by the action of viscous forces and eventually reach the region (3), leaving the domain. Notably, the pressure difference constitutes a critical output variable evaluated from the surface-averaged static pressure in the duct inlet and outlet.

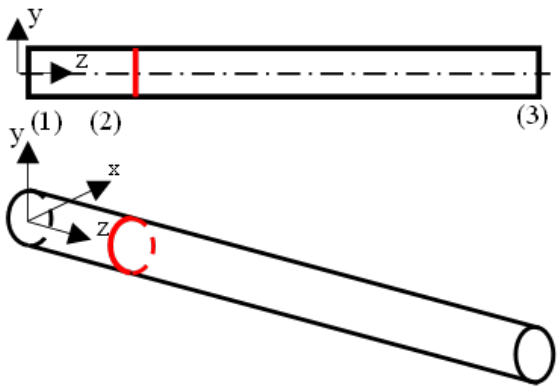

Figure 2: Capillary tube representing the problem geometry. The red circle is the solids injection surface located at 100 *mm* downstream the tube inlet to assure fully developed flow conditions.

The mathematical formulation presented in this study regards an Euler-Lagrange approach for a two-phase solid-liquid flow with four-way interactions between phases. Scale crystals compose the solid phase, considered as discrete

*Corresponding Author, Vinicius Gustavo Poletto vpoletto@utfpr.edu.br

non-deformable spheres. The particles are immersed in a uniform continuous liquid flow in an Eulerian approach. Mathematical expressions represent the forces resulting from the interactions of particles with the fluid or the contact with other particles. Each phase presents specific formulations, with information between the respective solutions accounted by coupling terms.

Assumptions refer to a laminar, incompressible, and isothermal flow without transferring heat or mass. As outlined later on, for the flow rate range considered, Reynolds number is not higher than 424. Particles are perfect spheres with rotational movement and friction effects disregarded to prioritize the simultaneous simulation of particle growth and adhesion, which poses many technical challenges. These simplifications are justified by the small particle size 20 μm for which rotational inertia and Magnus-type torques are negligible under creeping-flow conditions. Additionally, the assumption of perfect sphericity combined with the cohesive contact model provides an inherent mechanism of energy dissipation during agglomeration and separation, partially capturing effects typically associated with friction.

The balance equations for the multiphase flow account for the addition of the fluid volumetric fraction ϵ_β [-] and the coupling term for the interaction between phases $\boldsymbol{F}_{p\beta}$ [N/m^3] [22]. This way, the mass and momentum balance, represented respectively in Equations 1 and 2 are:

$$\frac{\partial \epsilon_\beta \rho_\beta}{\partial t} + \nabla \cdot (\epsilon_\beta \rho_\beta \boldsymbol{u}_\beta) = 0, \tag{1}$$

$$\frac{\partial \epsilon_\beta \rho_\beta \boldsymbol{u}_\beta}{\partial t} + \nabla \cdot (\epsilon_\beta \rho_\beta \boldsymbol{u}_\beta \boldsymbol{u}_\beta) = -\epsilon_\beta \nabla p_\beta + \nabla \cdot \tau_\beta + \epsilon_\beta \rho_\beta \boldsymbol{g} + \boldsymbol{F}_{p\beta}, \tag{2}$$

where ρ_β [kg/m^3] represents the fluid specific mass, t [s] is time, $\boldsymbol{u}_\beta$ [m/s] the fluid velocity, p_β [Pa] the fluid pressure, τ_β [N] the viscous stress tensor and $\boldsymbol{g}$ [m/s^2] the gravity acceleration. Note that in the absence of solids, as $\epsilon_\beta = 1$ and $\boldsymbol{F}_{p\beta} = 0$, the balance equations recover the Navier-Stokes ones for monophasic fluid flow.

A lagrangian reference frame accounts for each particle individually. The velocity $\boldsymbol{u}_{p[j]}$ [m/s] and the position $\boldsymbol{x}_{p[j]}$ [m] of a particle denoted by the index j are obtained by Equations 3 and 4, as follows:

$$\begin{aligned} m_p \frac{d\boldsymbol{u}_{p[j]}}{dt} = \sum \boldsymbol{F}_{p[j]} = &\boldsymbol{F}_{g[j]} + \boldsymbol{F}_{by[j]} + \boldsymbol{F}_{d[j]} + \boldsymbol{F}_{vm[j]} + \\ &\boldsymbol{F}_{pg[j]} + \boldsymbol{F}_{sl[j]} + \boldsymbol{F}_{col[j]} + \boldsymbol{F}_{adh[j]}, \end{aligned} \tag{3}$$

$$\boldsymbol{u}_{p[j]} = \frac{d\boldsymbol{x}_{p[j]}}{dt}, \tag{4}$$

being $m_{p[j]}$ [kg] the particle mass and $\sum \boldsymbol{F}_p[j]$ [N] the sum of all the acting forces on particle j. In the present work, rotational movement is not accounted for to simplify the simulation in terms of available computational time and power, even though adhesion plays significant effects over the sliding and rolling [23, 24]. A detailed mathematical description of the fluid-particle interaction forces is provided in [25].

To account for the effects of particle growth on phase interactions, one proposes a mathematical expression for the diameter d_p [m] indicated by Equation 5, where the particle diameter starts to grow at a rate defined as λ_t [mm/s] after reaching the terminal velocity:

$$d_p(t) = d_{p,0} + \lambda_t t. \tag{5}$$

Mathematical expressions relating the particle diameter to variables such as time, particle position in the flow domain, and composition, among others, are responsible for modeling particle growth. Particles can grow simultaneously or individually, allowing for a polydispersed system. Furthermore, if required, the model can also cover diameter reduction. In the present work, it is also considered the diameter resizing as a function of particle position, as defined in equation 6 by λ_p [mm/m].

*Corresponding Author, Vinicius Gustavo Poletto vpoletto@utfpr.edu.br

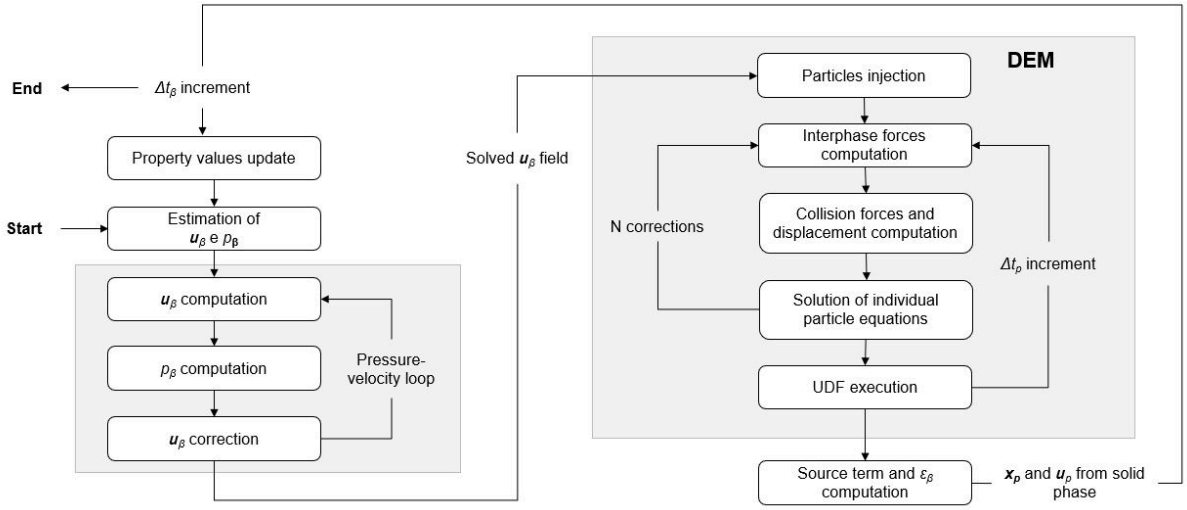

Figure 3: CFD-DEM numerical flowchart indicating features of the four-way coupling with the flow and particle properties. The implemented UDF to include growth and adhesion runs within the DEM loop after the solution of individual particles.

$$d_p(t) = d_{p,0} + \lambda_p z. \tag{6}$$

The adhesion model presented here considers only the van der Waals force of attraction between two bodies, relating it to material, size, and distance using Hamaker's model [26]. This simplification serves as an effective starting point for the model. This way, one creates a more manageable initial framework by concentrating on the primary adhesion mechanism and excluding the complexity of electrostatic forces. Integrating numerous parameters from the outset would necessitate extensive adjustments, resulting in significantly longer simulation times. Starting with a simpler model enables a more efficient refinement process before incorporating electrostatic forces. The cutoff distance a_{lim} [nm] is chosen to represent the range where electrostatic forces would predominate, thus providing a reasonable approximation for initial analysis. Therefore, for two spheres of the same diameter d_p [m], separated by a distance a [m] between surfaces, Equation 7 represents the attraction force. When a approaches zero, a cut-off distance a_{lim} [nm] bounds the adhesion intensity to avoid the singularity. A similar expression holds valid for particle-wall interactions.

$$\boldsymbol{F}_{adh[j]} = \begin{cases} -H\frac{d_p}{24a_{lim}^2} & \text{if } a \le a_{lim} \\ -H\frac{d_p}{24a^2} & \text{if } a > a_{lim} \end{cases} \tag{7}$$

Numerical modeling

As described in Section 2, the hybrid Euler-Lagrange approach to model the liquid-solid flow with adhesion and particle growth results in a segregated and coupled system of equations for each phase. Such a system of equations requires updating the velocity and position of each particle with contact interactions computed by the Discrete Element Method (DEM) proposed by [15]. Fluid domain equations resort to the Finite Volume Method to solve pressure and velocity fields [27]. Both models run separately but coupled, as displayed in the flowchart of Figure 3 by a recursive exchange of information. In the case of DEM, a particle-based meshless method [28], the simulation becomes lengthy as the number of equations increases with the number of particles in the domain. The numerical procedure starts by mapping the relative current position and identifying potential contacts. Upon identifying a contact, contact models computes the collision force in normal contact direction to decelerate particles during inbound.

*Corresponding Author, Vinicius Gustavo Poletto vpoletto@utfpr.edu.br

Modeling validation and verification

The work of Poletto et al. [29] discusses verification and validation results in terms of particle sedimentation, normal collision, oblique collision, and stack formation. In the presen work, verification results for the terminal velocity of a bead subjected to diameter growth are simulated. [30] experimentally measured the bead velocity over time, letting a bead immersed in a viscous fluid accelerates from rest and reaches the terminal velocity. Poletto et al. [31] presented a detailed mesh test concluding that a mesh element twice the diameter produces proper results. Poletto et al. [29] discusses the numerical reproduction of experimental results employing a simulation domain comprised of a box-shaped with dimensions 0.5 x 0.5 x 1.0 [m] discretized with 8 mm-sized elements using a uniform hexahedral mesh.

Effects of particle growth on fluid-particle interaction forces, shown in Figure 4 (a), aimed to verify whether the terminal velocities coincide after increasing the diameter over time by the acceleration curve for a particle whose initial diameter is $d_{p,0}$ = 2.0 mm and the final is $d_{p,f}$ = 4.0 mm, with a density of ρ_p = 7670 kg/m^3. Dashed lines represent settling velocities measured experimentally by [30]. Particle growth begins at t_{IP} = 0.4 s, after achieving the terminal velocity for the initial diameter $d_{p,0}$. Considering growth rates λ= 4, 10, and 20 mm/s, Figure 4b shows the increase in diameter over time, with the corresponding acceleration curves. The selected rates resemble a scenario where a particle resizes its diameter between values whose terminal velocities were measured experimentally and within a time window for a 1m-depth tank. In fact, crystal growth rates due to mass diffusion or heterogeneous nucleation typically range in the order of nanometers per second. However, such values would not provide significant answers for the sensitivity analysis. The diameter change at t_{IP} = 0.4 s provokes a practically instantaneous increase in the velocity for all values of λ. The growth rate modifies the time required for achieving the new terminal velocity, as seen by the elongated velocity curves for lower values of λ in Figure 4a. Nevertheless, the final value attained for all cases is virtually the same, which approaches the experimental settling velocity for $d_{p,f}$, indicating excellent consistency of the model in evaluating different growth conditions. Noteworthy is the lack of available experimental values in the [30] study matching the exact conditions of the particle after growth. Thus, the slight difference in density for the experimental (ρ_p = 7700 kg/m^3) and simulation (ρ_p = 7670 kg/m^3) cases explains the subtle velocity deviation from the experimental results for d_p = 4.0 mm in Figure 4a.

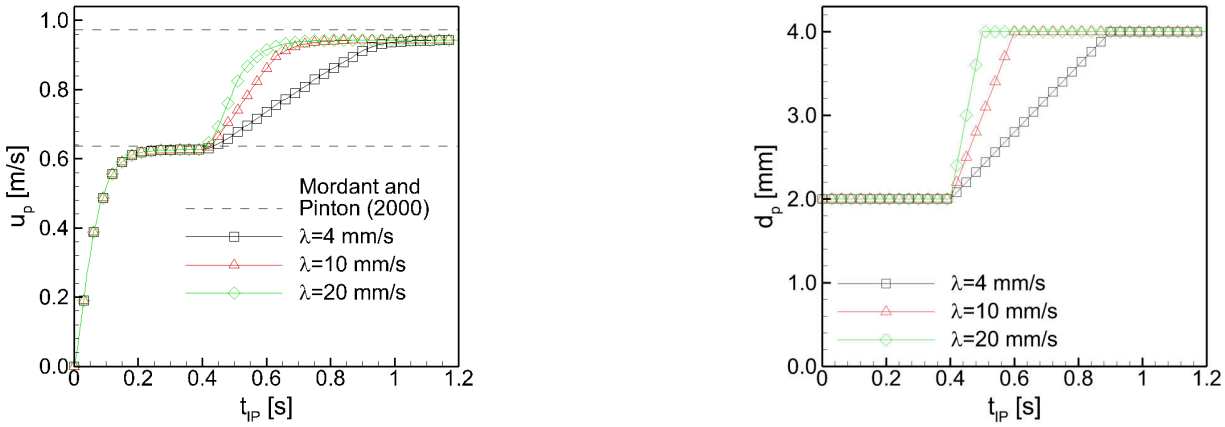

(a) **(b)**

Figure 4: Inclusion of the diameter growth from 2.0 mm to 4.0 mm on the settling velocity results: (a) settling velocity as a function of the growth rate, and (b) diameter as a function of the growth rate. CFD-DEM reproduced properly the settling velocity for both the initial and final diameter, indicating that fluid-particle interaction forces are updated with the increment in diameter.

Verification of DEM contact force calculations is performed by reproducing the results of the normal collision study of [32], as detailed by Poletto et al. [29]. The study evaluated the velocity of a Teflon particle of diameter d_p = 6.0 mm and density ρ_p = 2150 kg/m^3 immersed in air at ambient conditions (1.2×10^{-3} kg/m^3 and 1.85×10^{-5} Pa.s) colliding successively with a horizontal surface. To address the effect of adhesion over the force balance of a particle in contact with a wall, the normal collision test is rerun in terms of the magnitude of the adhesive force χ [-] implemented by the UDF and defined in Equation 8:

*Corresponding Author, Vinicius Gustavo Poletto vpoletto@utfpr.edu.br

$$\chi = \frac{|F_{adh[j]}|}{|F^1_{max,col[j]}|} \tag{8}$$

where $F_{adh[j]}$ [N] is the adhesive force . For instance, χ= 0.5 represents an adhesive force whose magnitude is half the collision force's maximum value. Despite the results being discussed in terms of χ, it correlates with the cut-off distance of the Hamaker model. Figure 5 demonstrates the influence of adhesion over the colliding particle velocity. Considering a Hamaker's constant of $H = 2.75 \times 10^{-20}$ J for Teflon [33], χ ranges from 0 to 3. The increment in χ increases the damping effect of the collision, as seen by the lower velocity u_p values achieved in the ensuing collisions.

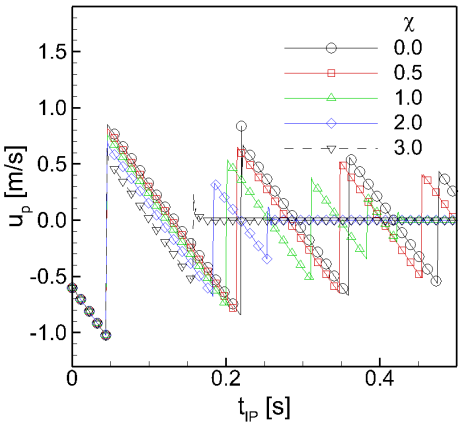

Figure 5: Inclusion of the adhesive force χ on a particle colliding normally over a flat surface in terms of the acceleration curve as a function of the adhesion intensity χ.

Adhesion and growth in a capillary tube

This section investigates the problem posed in Section 2. The influence of particle growth and adhesion is performed according to four scenarios. The first considers the flow with dispersed particles to observe the flow effect in the absence of growth and adhesion. The second scenario analyzes particle transport's pattern and temporal evolution subjected to diameter resizing (growth) as a function of the axial position. The third scenario investigates the effects of particulate adhesion throughout the flow and the eventual formation of agglomerates. Simultaneous effects of particle growth and adhesion are then considered in the fourth scenario.

The proposed mesh for all simulated cases of particle growth and adhesion is displayed in Figure 6. Given the high ratio between the tube cross-section and the largest simulated particle of 40 μm, element refinements near the wall could easily compromise the simulation convergence as the fluid volumetric fraction approaches zero, especially due to the adhesion force that keeps particles near the wall. To address this, a mesh study was conducted to ensure that the ϵ_β remained no higher than 0.75 at all times while maintaining the fluid flow solution as close to the analytical one as possible. Since the flow rate Q_β = 10 mL/min results in laminar flow, approximately uniform elements of size 40 μm without refinement near the wall yielded satisfactory results for both phases, resulting in a total of 5.4×10^4 elements for the proposed geometry.

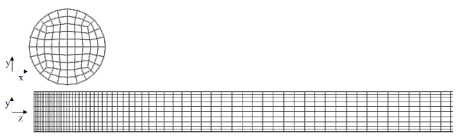

Figure 6: Capillary tube mesh for adhesion and growth simulations.

The fluid viscosity and specific mass, as well as the other parameters, are summarized in Table 1. The range of flow rate

*Corresponding Author, Vinicius Gustavo Poletto vpoletto@utfpr.edu.br

Q_β yields in a Reynolds number Re varying from 106 to 424 assuring the laminar regime. The particle-to-fluid specific mass ratio, $\rho_{p/\beta}$= 4.5, represents barium sulfate. Particles' diameter is 30 μm, but in cases with resizing, the diameter increases from 20 μm up to 40 μm with a constant growth rate of 0.0213 μm/mm, as defined by Equation 6. Likewise, as described in the sedimentation with particle resizing verification test, the chosen growth rate yields visual results for the time window allowed by the residence time. The adhesive force ratio is χ=5×10^4. Noteworthy, as particles grow, the solid phase concentration varies along the simulation since the specific mass is constant.

Fluid			
Dynamic viscosity	μ	0.001	[Pa.s]
Specific mass	ρ_β	1000	[kg/m^3]
Flow rate	Q_β	2.5;5;10	[mL/min]
Reynolds number	Re	106; 212; 424	[-]
Time step	Δt_β	5×10^{-4}	[s]
Particle			
Fluid specific mass ratio	$\rho_{p/\beta}$	4.5	[-]
Fluid specific mass	ρ_β	1000	[kg/m^3]
Number of injection points	n_{IP}	59	[-]
Time step	Δt_p	1×10^{-7}	[s]
Injection rate	N_p	118	[Part/s]
Injection velocity	$v_{p,IP}$	$2u_{\beta,max}$	[m/s]
Restitution coefficient	$e_{pp/pw}$	0.75; 0.9	[-]
Diameter	d_p	30	[μm]
Adhesive force ratio	χ	5×10^4	[-]
Growth characteristics			
Starting diameter	$d_{p,0}$	20	[μm]
Final diameter	$d_{p,f}$	40	[μm]
Starting position	z_0	150	[mm]
Final position	z_f	620	[mm]

Table 1: Summary of simulation parameters for liquid-solid flow in a capillary tube.

A stable and concise particle injection condition obtained for n_{IP}=59 injection points uniformly distributed in the duct cross-section provided an injection rate of N_p=118 particles/s. Simulations without the adhesion force resulted in approximately 4500 particles in the domain at quasi-steady-state. The simulated 0.2 s took 30 days of processing on a single-core Intel Xeon Gold 6230 CPU at 2.10 GHz. The Rayleigh time considering $k_n = 400\ N/m$ leads to 4.34 μs, while the contact time supposing a top speed of 1.7 m/s is 1.47 μs. The chosen time step is less than 10% of such values, meaning that the time is integrated at least ten time in each contact.

Results for flow rate Q = 10mL/min, displayed in Figure 7a, consider the transport of solids in the absence of adhesion and resizing, with particles colored as a function of the velocity magnitude. In fact, 30μm particles show a dispersed pattern close to the 59 injection points, then settle down and roll out of the domain, close to the outlet. In Figure 7b, solids are dispersed close to the injection points, but as diameter resizing turns particles heavier, they also hit the wall downstream the case without resizing, as expected, and roll out. Figure 8 shows the dimensionless pressure P_β, referenced to the one-phase flow pressure difference, over the particle injection period that starts at t_{IP} =0 s, following the convergence of the fluid flow solution. For the dispersed flow, without growth or adhesion, there is a slight increase of P_β at 0.05 s accounting for the pressure drop imposed by the solids. The particle resizing scenario shows a similar trend; despite increasing the diameter from 20 μm to 40 μm, the mean diameter remains 30 μm. Such conditions indicate that four-way coupling in CFD-DEM is capable of experiencing fluid-particle interactions as the diameter changes over time. Typical growth rates for crystals are in the 10^{-9} m/s order [34]. In the present problem, growth rates are overestimated, leading to a more challenging numerical scenario to achieve convergence and stability. In Figure 7c the inclusion of adhesion indicates deposition over the walls covering about half of the tube length. Downstream, particles eventually pile up and build agglomerates whose size ranges from 0.10 to 0.15 mm. These cluster remain motionless adhered to the wall, as suggested by the dark blue color. The velocity magnitude field u_β at the longitudinal

*Corresponding Author, Vinicius Gustavo Poletto vpoletto@utfpr.edu.br

cross section also indicates a wavy pattern for the color gradient close to the wall and the fluid acceleration in the duct center. The dimensionless pressure uptrend, shown in Figure 8 is a consequence of the increasing solid mass inside the domain.

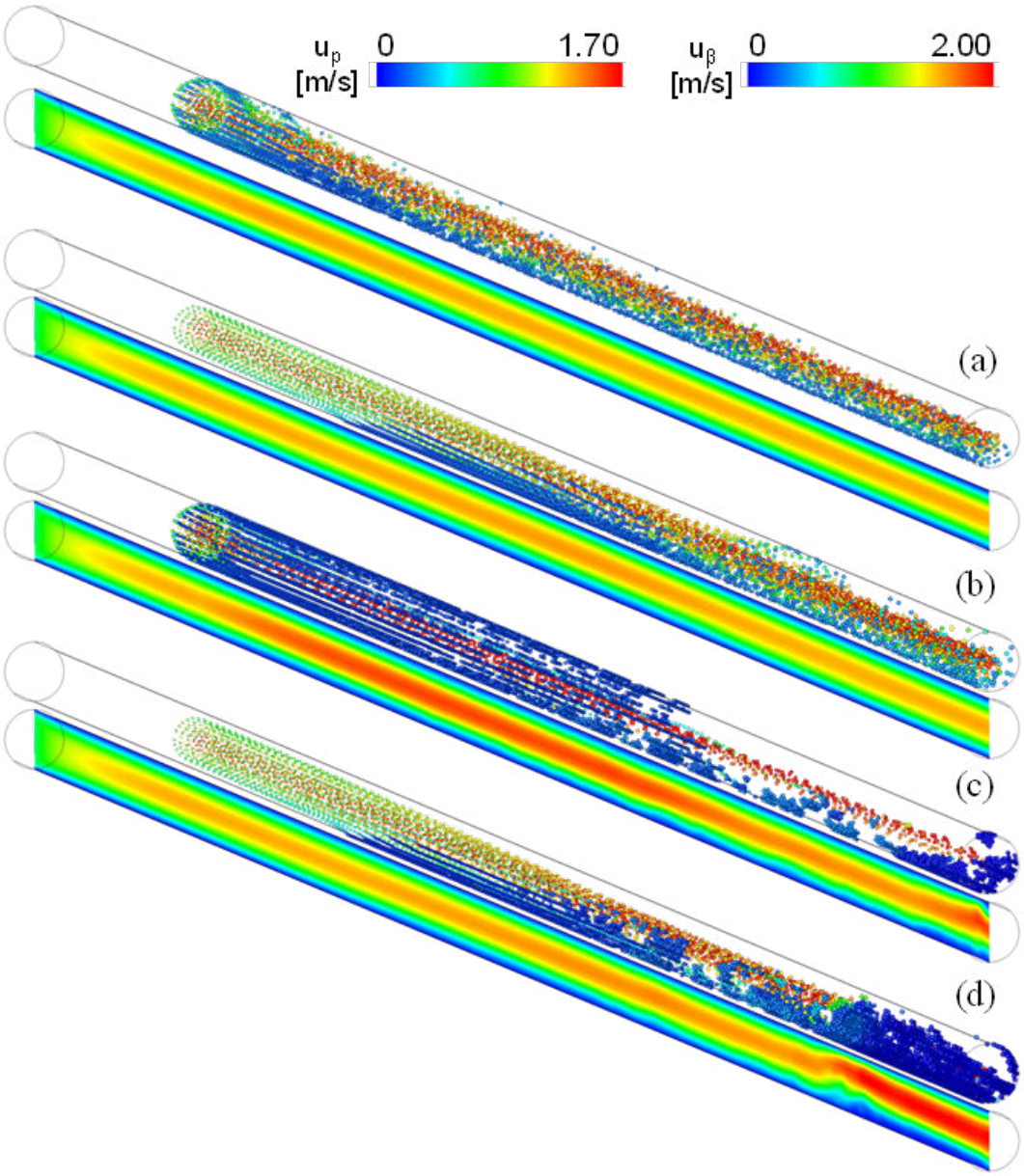

Figure 7: Liquid-solid flow in a capillary tube with flow rate Q= 10 mL/min. Comparison of transport patterns for (a) 30 μm particles; (b) particles resizing from 20 μm to 40 μm; (c) 30 μm particles with adhesion; (d) particle resizing from 20 μm to 40 μm with adhesion.

Results combining adhesion and growth are shown in Figure 7d. Particles recently injected have 20 μm and remain dispersed. In fact, the velocity magnitude field in this region seems untouched. Recalling that the diameter increases as a function of axial position, particles becomes heavier and settle down, building larger cluster with size varying from 0.15 to 0.25 mm. The u_β field clearly indicates disturbances close to the outlet where agglomerates are larger. The P_β curve in 8 begins to increase steeply at 0.05 s and show an intense increment with oscillations that are a consequence of

*Corresponding Author, Vinicius Gustavo Poletto vpoletto@utfpr.edu.br

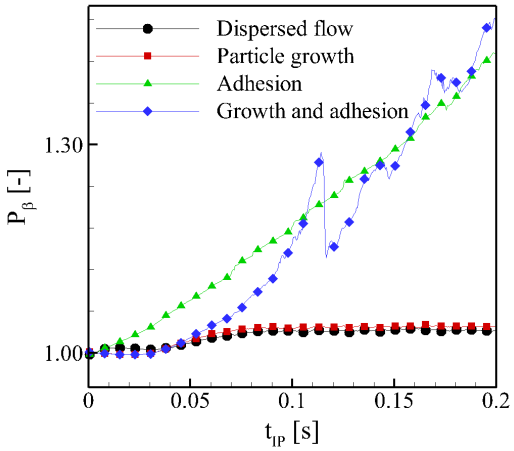

Figure 8: Dimensionless pressure P_β, normalized by the single-phase pressure drop, for Q = 10 ml/min comparing flow patterns of dispersed particulate flow, particle growth from 20 μm to 40 μm, adhesion, and growth and adhesion combined.

relieving the pressure difference. In fact, the contact area of the agglomerate with the wall is not enough to balance the drag imposed by the flow that washes the bulk bodies away.

Results in Figure 10 consider growth and adhesion combined in the light of the influence of the flow rate, assuming 2.5, 5.0, and 10.0 mL/min. Two phenomena co-occur with the increase in flow rate. The first relates to particle dispersion that hampers the formation of clusters. In this case, for a constant injection rate, the increment in flow rate would increase the relative distance between particles, reducing the solids concentration. The second effect refers to the growth process, which starts earlier for faster particles. Recalling that the growth rate is constant 0.0213 μm and the diameter varies with the position, according to Equation 6). For Q = 2.5 mL/min, particles remain closer to each other, eventually colliding and creating agglomerates that roll out the tube. As particles move slower, growth helps to bulk the already-built agglomerates. The dimensionless pressure response, now referenced in terms of the one-phase pressure difference of the respective flow rate, shown in Figure 10 has a similar trend than observed for Q_β = 10.0 mL/min. For Q = 5.0 mL/min, it seems that the growth and adhesion converge to the establishment of bulk agglomerates, with particles settling near the same position on the tube. In this case, agglomerates have the same order of dimension of the capillary diameter, therefore imposing the pressure outbreak observed in Figure 10. Such effects show the four-way CFD-DEM coupling capability of simulating interesting phenomena associated with particulate flows.

Final considerations

In the present work, an Euler-Lagrange hybrid formulation to model liquid-solid two-phase flow with adhesion and particle growth has been proposed. The two-way coupling CFD-DEM available in the commercial package Ansys Fluent is customized using a user-defined function to include the particle growth and adhesion effects. Results on the liquid-solid flow with particle growth and adhesion are presented in a capillary tube, elucidating the effect of each phenomenon occurring isolated as well as combined. The main findings of this work, summarized as follows, indicate the proposed model can handle the particle growth and adhesion simultaneously for representing the inorganic scale formation:

In terminal velocity tests, results for a particle growing from 2 to 4 mm show that the fluid-particle interaction presents a relative error of 3% even with the diameter increment. In normal collision simulations, as expected, an increase in the adhesion magnitude increases the particle's ability to adhere to the surface and exponentially decreases the time required for complete adhesion.

The model handles combined adhesion and growth in a viscous flow. The comparison between the four scenarios resulted in distinct transport patterns, highlighting that each effect is successfully accounted for within the scope of CFD-DEM modeling. The possibility of observing particles interacting with each other helps in understanding phenomena that are not clearly depicted solely by a pressure difference response.

*Corresponding Author, Vinicius Gustavo Poletto vpoletto@utfpr.edu.br

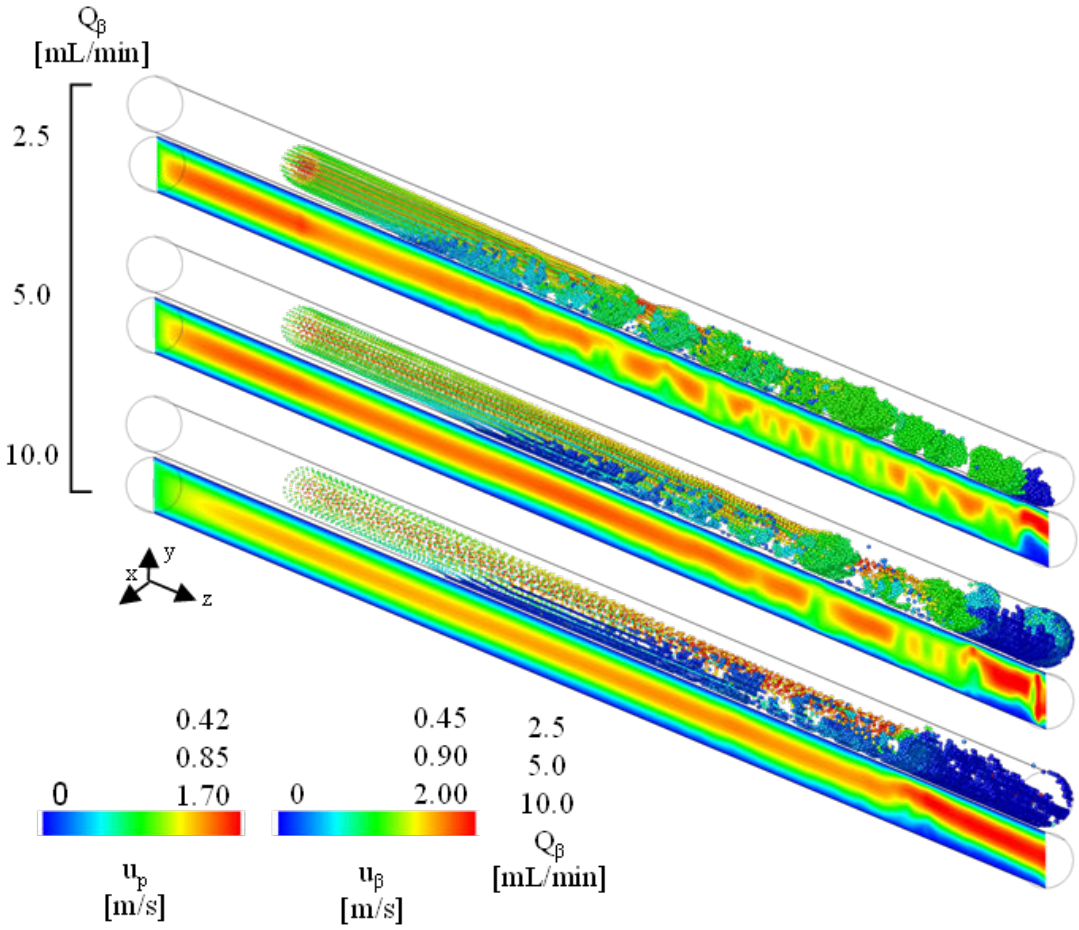

Figure 9: Effect of flow rate over combined adhesion and particle growth; parameters of Table 1.

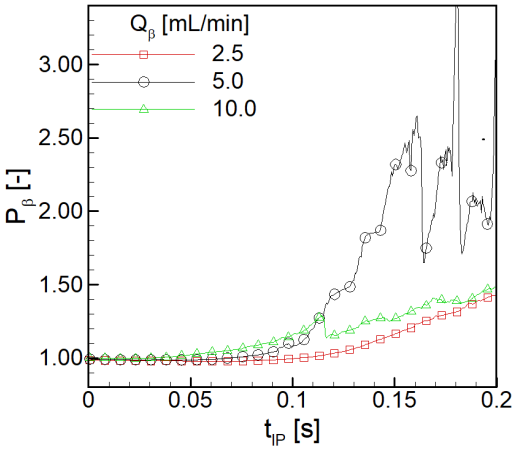

Figure 10: Effect of flow rate: dimensionless pressure P_β as a function of time, normalized by the single-phase pressure drop.

*Corresponding Author, Vinicius Gustavo Poletto vpoletto@utfpr.edu.br

The influence of the flow rate is reflected in the agglomerate build-up process, possibly creating a favorable condition for bulky bodies whose scale is the capillary diameter. Finally, the proposed model was able to capture the competitive effect between particle growth, which occurs faster as the flow rate increases, and the solids concentration, which decreases as the flow rate increases.

Acknowledgments

The authors are grateful to the Brazilian Petroleum Agency (ANP), the Human Resources Program for the Petroleum and Gas Sector PRH-ANP (PRH21.1 - UTFPR), and CENPES-PETROBRAS for the provided financial support.

References

[1] Hong-Qing Jin, Shantanu Shahane, Yuheng Zhang, Sophie Wang, and Kashif Nawaz. Modeling of crystallization fouling on a horizontal-tube falling-film evaporator for thermal desalination. *International Journal of Heat and Mass Transfer*, 178:121596, 2021.

[2] Jörg Zotzmann, Nele Hastreiter, Sathish Mayanna, Thomas Reinsch, and Simona Regenspurg. A fibre-optical method for monitoring barite precipitation at high pressure/high temperature conditions. *Applied Geochemistry*, 127:104906, 2021.

[3] Sassan Hajirezaie, Xingru Wu, Mohamad Reza Soltanian, and Sarah Sakha. Numerical simulation of mineral precipitation in hydrocarbon reservoirs and wellbores. *Fuel*, 238:462–472, 2019.

[4] V. Eroini, A. Neville, N. Kapur, and M. Euvrard. New insight into the relation between bulk precipitation and surface deposition of calcium carbonate mineral scale. *Desalination*, 51(4-6):882–291, 2013.

[5] H. Du and E. Amstad. Water: How does it influence the caco3 formation? *Angewandte Chemie - International Edition*, 59(5):1798–1816, 2019.

[6] Martin Iggland and Marco Mazzotti. Population balance modeling with size-dependent solubility: Ostwald ripening. *Crystal growth & design*, 12(3):1489–1500, 2012.

[7] I. J. McPherson, M. Peruffo, and P. R Unwin. Role of mass transport in the deposition, growth, and transformation of calcium carbonate on surfaces at high supersaturation. *Crystal Growth and Design*, 22(8):4721–4729, 2022.

[8] O. Sanni, Kabir Raheem, A. Neville, and T. Charpentier. Surface precipitation and growth kinetics of calcium carbonate (caco3) scale using a novel capillary flow rig. In *Corrosion Virtual Conference and Expo*, number 16560, pages 1–15. Association for Materials Protection and Performance (AMPP), 2021.

[9] Musa Mpelwa and Shan-Fa Tang. State of the art of synthetic threshold scale inhibitors for mineral scaling in the petroleum industry: a review. *Petroleum Science*, 16(4):830–849, 2019.

[10] ASA Fadairo, O Omole, and O Falode. A modified model for predicting permeability damage due to oilfield scale deposition. *Petroleum science and technology*, 27(13):1454–1465, 2009.

[11] Marko Trampuž, Dušan Teslić, and Blaž Likozar. Crystallization of fesoterodine fumarate active pharmaceutical ingredient: Modelling of thermodynamic equilibrium, nucleation, growth, agglomeration and dissolution kinetics and temperature cycling. *Chemical Engineering Science*, 201:97–111, 2019.

[12] R. P. Cosmo, F. A. R. Pereira, D. C. Ribeiro, W. Q. Barros, and A. L. Martins. Estimating co2 degassing effect on caco3 precipitation under oil well conditions. *Journal of Petroleum Science and Engineering*, 181:106207, 2019.

[13] R. P. Cosmo, F. A. R. Pereira, E. J. Soares, and A. L. Martins. Modeling and validation of the co2 degassing effect on caco3 precipitation using oilfield data. *Fuel*, 310:122067, 2022.

[14] P. Zhang, Y. Liu, S. C. Kuok, A. T. Kan, and M. B. Tomson. Development of modeling approaches to describe mineral scale deposition kinetics in porous medium and pipe flow system. *Journal of Petroleum Science and Engineering*, 178:594–601, 2019.

*Corresponding Author, Vinicius Gustavo Poletto vpoletto@utfpr.edu.br

[15] Peter A Cundall and Otto DL Strack. A discrete numerical model for granular assemblies. *geotechnique*, 29(1): 47–65, 1979.

[16] Yutaka Tsuji, Toshihiro Kawaguchi, and Toshitsugu Tanaka. Discrete particle simulation of two-dimensional fluidized bed. *Powder technology*, 77(1):79–87, 1993.

[17] V. G. Poletto, M. E. Mazuroski, F. R. A. Pereira, M. P. Schwalbert, M. V. Duarte Ferreira, T. H. T. Eduardo, F. C. De Lai, S. L. M. Junqueira, and A. L. Martins. Hydrodynamic simulation supports scale formation in technical specification for downhole equipment. In *SPE International Oilfield Scale Conference and Exhibition*. OnePetro, 2022.

[18] Juan Ramirez, Martijn de Munck, Zhitao Liu, David Raphael Rieder, Maike Baltussen, Kay Buist, and Johannes AM Hans Kuipers. Cfd-dem evaluation of the clustering behavior in a riser– the effect of the drag force model. *Industrial & Engineering Chemistry Research*, 2023.

[19] Nazerke Saparbayeva, Yu-Fen Chang, Pawel Kosinski, Alex C Hoffmann, Boris V Balakin, and Pavel G Struchalin. Cohesive collisions of particles in liquid media studied by cfd-dem, video tracking, and positron emission particle tracking. *Powder Technology*, 426:118660, 2023.

[20] AS Dogonchi, SM Seyyedi, M Hashemi-Tilehnoee, and DD Ganji. Investigation of sedimentation process of soluble spherical particles in a non-newtonian medium. *Journal of colloid and interface science*, 530:532–537, 2018.

[21] Avi Uzi, Gal Beit Halevy, and Avi Levy. Cfd-dem modeling of soluble nacl particles conveyed in brine. *Powder Technology*, 360:1278–1294, 2020.

[22] B Popoff and M Braun. A lagrangian approach to dense particulate flow. In *6th International Conference on Multiphase Flow, ICMF 2007*, pages 510–521, Leipzig, 2007.

[23] C Dominik and AGGM Tielens. Resistance to rolling in the adhesive contact of two elastic spheres. *Philosophical Magazine A*, 72(3):783–803, 1995.

[24] Jeffery S Marshall and Shuiqing Li. *Adhesive particle flow*. Cambridge University Press, 2014.

[25] Marina Elizabeth Mazuroski, Thiago Machado Neubauer, Vinicius Gustavo Poletto, Fernando Cesar De Lai, Bruno Barbosa Castro, André Leibsohn Martins, and Silvio Luiz de Mello Junqueira. CFD–DEM modeling of particle clustering and deposition combining growth and adhesion. *Journal of the Brazilian Society of Mechanical Sciences and Engineering*, 48(72):72, 2026. doi: 10.1007/s40430-025-06061-3.

[26] Hugo C Hamaker. The london—van der waals attraction between spherical particles. *physica*, 4(10):1058–1072, 1937.

[27] S V Patankar and D B Spalding. A calculation procedure for heat, mass and momentum transfer in three-dimensional parabolic flows. *International Journal of Heat and Mass Transfer1*, 5(1787-1806), 1972.

[28] HP Zhu, ZY Zhou, RY Yang, and AB Yu. Discrete particle simulation of particulate systems: theoretical developments. *Chemical Engineering Science*, 62(13):3378–3396, 2007.

[29] V. G. Poletto, F. C. De Lai, and S. L. M. Junqueira. Cfd–dem simulation of mud cake formation in heterogeneous porous medium for lost circulation control. *Journal of the Brazilian Society of Mechanical Sciences and Engineering*, 42(7):1–16, 2020.

[30] Nicolas Mordant and J-F Pinton. Velocity measurement of a settling sphere. *The European Physical Journal B-Condensed Matter and Complex Systems*, 18(2):343–352, 2000.

[31] V.G. Poletto, V. S. L. Barros, F. C. De Lai, and S. L. M. Junqueira. Euler-lagrange numerical simulation for particulate flow using ddpm-dem (in portuguese). In *ENEMP 2017*, 2017.

[32] P Gondret, M Lance, and L Petit. Bouncing motion of spherical particles in fluids. *Physics of fluids*, 14(2): 643–652, 2002.

*Corresponding Author, Vinicius Gustavo Poletto vpoletto@utfpr.edu.br

[33] Jacob N Israelachvili. *Intermolecular and surface forces*. Academic press, 2011.

[34] Thiago Machado Neubauer, Fabiane Santos Serpa, Elton Franceschi, Claudio Dariva, Claudia Sayer, Pedro Henrique Hermes de Araújo, Bruno Barbosa Castro, Wagner Aldeia, and Cristiane da Costa. Crystallization of calcium carbonate: Modeling thermodynamic equilibrium, pathway, nucleation, growth, agglomeration, and dissolution kinetics with the presence of mg2+, ba2+, and sr2+. *Industrial & Engineering Chemistry Research*, 61(37): 13944–13961, 2022.

*Corresponding Author, Vinicius Gustavo Poletto vpoletto@utfpr.edu.br

Machine Learning-Based Prediction of Non-Spherical Particle Agglomeration

[1]Connor Nolan*; [2]Lee Mortimer; [3]Peter Jimack; [2]Michael Fairweather

[1]*EPSRC Centre for Doctoral Training in Future Fluid Dynamics, University of Leeds, Leeds LS2 9JT, UK*

[2]*School of Chemical and Process Engineering, University of Leeds, Leeds LS2 9JT, UK*

[3]*School of Computer Science, University of Leeds, Leeds LS2 9JT, UK*

Keywords: Particle-laden flow: Non-spherical; Agglomeration; Classification

Abstract. Interactions between ellipsoidal particles in turbulent and shear flows are common both in industry and nature. Such interactions give rise to a range of phenomena such as agglomeration, deposition and clogging. This work presents a comparative machine learning framework for predicting the agglomeration of prolate ellipsoid particles in a shear flow between parallel moving plates. A dataset of 200 high-fidelity immersed boundary method (IBM) simulations is used as training data, where each simulation fully resolves the binary collision of two prolate ellipsoids. Agglomeration is accommodated within the IBM framework through attractive van der Walls forces adapted to consider the orientational dependencies associated with the non-spherical shape. The features included in the training data are the relative translational and angular velocities, spatial offsets, particle orientations (quaternions), and wall speed as a proxy for shear rate. The models considered in this work are logistic regression, random forest, a support vector machine (RFB) and a simple multilayer perceptron. The inclusion of new features quantifying relative position and alignment lead to a significant increase in accuracy, with the random forest method being the best classifier given the parameters of this study.

1. Introduction

Turbulent particle-laden flows are ubiquitous in industrial and natural settings, with particles frequently being highly non-spherical and subject to inter-particle collisions that give rise to agglomeration, deposition, and clogging [1, 2]. Understanding and predicting these phenomena is of particular importance in safety-critical applications such as nuclear waste transport, where the consequences of process failure are severe.

The simulation of particle-laden turbulent channel flow has a long history, with much of the literature focusing on spherical particles using point-particle methodologies, generating key insights into preferential concentration and turbophoresis [3, 4]. Non-sphericity can be incorporated within point-particle frameworks [5, 6], but often requires complex empirical force correlations and simplified collision models. Fully resolved approaches such as the immersed boundary method (IBM) [7] overcome these limitations by representing the particle geometry explicitly, providing high accuracy at the cost of substantially increased computational expense [8].

Agglomeration modelling within point-particle and discrete element frameworks typically relies on simplified single-timestep energy criteria to determine collision outcomes [9, 10]. These approaches reproduce bulk behaviour but cannot capture the time-dependent dynamics or morphological complexity of the agglomeration process. DLVO theory [11, 12], which balances attractive van der Waals and repulsive electric double layer forces, provides a more physically complete description. Its integration into IBM simulations has enabled high-fidelity modelling of agglomeration between non-spherical ellipsoidal particles [8].

Despite their accuracy, the computational cost of DLVO-informed IBM simulations remains prohibitive for large-scale engineering applications. Machine learning (ML) offers a promising alternative, with recent studies demonstrating its efficacy in predicting particle drag coefficients and reconstructing particle trajectories in wall-bounded turbulence at unseen Reynolds numbers [13, 14]. However, its application to particle agglomeration remains sparse. The challenge lies in the high dimensionality of the feature space where collision outcome depends not only on translational kinetic energy but also on the

relative orientational alignment of the particles and the local flow, making pattern recognition non-trivial.

In this work, a dataset of 200 high-fidelity IBM simulations of prolate ellipsoid collisions, constructed to be representative of those observed in turbulent channel flow at , is used to train and compare a range of ML classifiers. Feature importance analysis is employed to identify the physical conditions most strongly associated with agglomeration, providing both a predictive tool and fundamental insight into the collision dynamics of non-spherical particles.

2. Methodology

2.1 Fluid phase modelling

The carrier phase is computed via direct numerical simulation of the incompressible Navier-Stokes equations using the spectral element method. This study leverages the open-source flow solver Nek5000 [15]. The computational domain is a small 0.75 mm cube comprised of 2160 ($12\times12\times15$) elements, with refinement close to the walls. Each element uses seventh-order Lagrange interpolants on Gauss-Lobatto-Legendre nodes, giving approximately 0.75 million equivalent grid points. A plane Couette flow configuration is considered to impose constant shear. The cubic domain has periodic conditions in the streamwise (and spanwise directions with no-slip moving walls in the wall-normal (direction, with the walls given equal and opposite velocities.

2.2 Immersed boundary method

The non-spherical particles are modelled using an icospherical mesh with 320 triangular faces, scaled along the principal *x*-axis to create a prolate spheroid with constant 2.5:1 aspect ratio. The coupling between the particles and the fluid follows the method outlined in [5, 8]. In this method the no-slip condition on the particle's surface is enforced by a ghost cell mirroring technique. The translational and rotational dynamics of the particles are governed by hydrodynamic forces and torques computed directly from the fluid pressure and viscous stress tensor. These contributions are interpolated onto the 320 faces of the icospherical particle mesh with a sum over all faces giving the total force and torque. The torque is then used to update the angular velocity of the particle by solving Euler's rotation equations in the particle reference frame. Further details may be found in [8].

Particle interactions are additionally governed by DLVO forces, which combine van der Waals attraction and electric double-layer repulsion, with the interaction strength depending on particle orientation and local surface curvature. Collision detection between nonspherical particles is performed using an adaptive common-normal method to identify the minimum separation distance and contact points. Collisions are resolved using a hard-sphere approach with momentum exchange based on Newton's third law and restitution effects, while lubrication forces are neglected due to the dominance of van der Waals interactions at the separations considered.

2.3 Training data generation

The training dataset consists of 200 binary collisions between prolate ellipsoids extracted from four-way coupled LPT simulations of a turbulent channel flow. For each collision, particle positions, translational and angular velocities, quaternions, and local fluid velocity gradient tensors were recorded. The velocity gradient tensors of both particles were averaged and decomposed into their strain-rate component, whose principal directions defined a local flow-aligned coordinate system. All relative kinematic quantities () and particle orientations () were rotated into this frame to form the IBM initial conditions.

The local shear rate and IBM domain half-height determined the wall speed . In the IBM simulations, the particles were initialised symmetrically about the origin using the relative separation, velocity, and angular velocity, while the top and bottom walls moved at velocities . Each simulation was run until the collision outcome could be identified.

Collision outcomes were classified by comparing the late-time minimum separation distance to the initial separation. Cases where the separation decreased to less than one fifth of its initial value were classified as agglomeration; otherwise, they were classified as bounce events. Of the 200 collisions considered, 53% resulted in agglomeration.

2.4 Feature engineering

The raw IBM collision inputs (, , , , and were transformed into a reduced set of physically meaningful features describing particle geometry and collision dynamics. Particle quaternions and were converted into world-space principal axes to compute alignment metrics , , and . The relative displacement vector was used to determine the separation distance and the normalised separation direction , from which facing metrics and and the interaction score were derived to quantify particle orientation during collision. The magnitudes of the relative translational and angular velocities, and , together with , were included to characterise collision intensity. Overall, the original 18 IBM parameters were reduced to 10 scalar features (, , , , , , , , , , capturing the dominant geometric and dynamic behaviour governing ellipsoidal particle collisions while significantly reducing the dimensionality of the parameter space.

2.5 Machine learning framework

The engineered dataset was used to train supervised machine learning classifiers for predicting the binary collision outcomes corresponding to agglomeration or rebound. Four classification approaches were investigated, namely Logistic Regression (LR), Random Forest (RF), Support Vector Machine with a radial basis function kernel (SVM-RBF) and a simple Multi-Layer Perceptron neural network (MLP). These models were selected to provide a comparison between linear, ensemble-based, kernel-based and nonlinear neural-network classifiers. All models were implemented using the Python scikit-learn library.

Feature standardisation using zero-mean unit-variance normalisation was applied for LR, SVM, and MLP models. Random Forest models were trained directly on the unscaled feature space due to their scale-invariant tree-based structure. Logistic Regression employed balanced class weighting with a maximum of 2000 optimisation iterations. The Random Forest classifier used 400 trees with a maximum depth of 2, minimum leaf size of 5, minimum split size of 10, and square-root feature sampling. The SVM model used an RBF kernel with probabilistic outputs enabled. The MLP classifier consisted of a single hidden layer containing four neurons with hyperbolic tangent activation and L2 regularisation (). Model performance was evaluated using stratified 5-fold cross-validation to preserve class balance across folds, with the accuracy, F1-score, and the area under the receiver operating characteristic curve (ROC-AUC) being used as evaluation metrics. For all models the test train split was set to 20%.

3. Results and Discussion

3.1 Feature space visualisation

Principal component analysis (PCA) was applied to the engineered feature set to provide a low-dimensional visualisation of our training set structure. The first two principal components and , account for 20.0% and 14.3% of the total variance respectively.

Figure 1 reveals partial but incomplete separation between agglomeration and bouncing events. A large cluster of both agglomerated and bounced data points is observed in the region , which suggests that no single linear combination of features can be used to cleanly distinguish collision outcome in this reduced space. We note that at higher values of the samples become sparse and skewed towards agglomeration events. The significant overlap in the centre region motivates the use of nonlinear classifiers capable of exploiting higher-dimensional feature interactions.

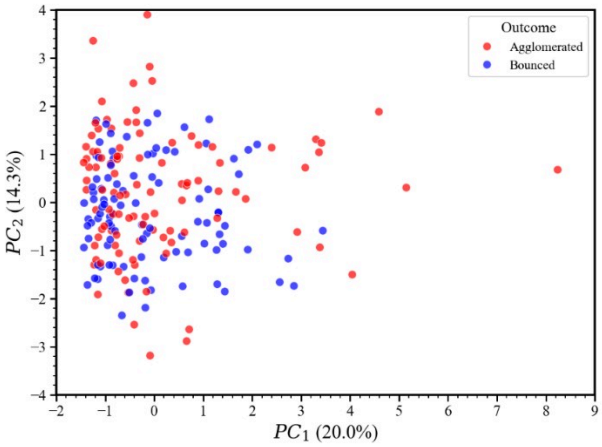

Figure 1: Principal component analysis of the engineered feature set, projected onto the first two principal components. Data points are coloured by collision outcome: agglomeration (red) and rebound (blue). PC_1 and PC_2 account for 20.0% and 14.3% of the total variance, respectively.

3.2 Classification performance

Tabel 1 summarises the classification performance of the four machine learning models to predict binary collision outcomes. The random forest model achieves the highest overall performance, with a ROC-AUC of 0.813, an F1-score of 0.759, and an accuracy of 0.76, indicating strong discriminative capability and robust generalisation across folds. The support vector machine with radial basis function shows intermediate performance outperforming the logistic regression, which suggests there may be some nonlinear structure within the feature space. The multi-layer perceptron shows the worst performance across all metrics. Overall, it is noted that the ensemble-based method demonstrates superior predictive performance compared to the linear and shallow neural network approaches, highlighting the importance of nonlinear feature interactions in determining collision outcome between non-spherical particles.

Table 1: Classification performance of machine learning models for predicting binary collision outcomes (agglomeration versus rebound), evaluated using ROC-AUC, F1-score, and accuracy.

Model	**ROC-AUC**	**F1-Score**	**Accuracy**
LR	0.739	0.656	0.670
RF	0.813	0.759	0.760
SVM-RBF	0.756	0.705	0.690
MLP	0.668	0.657	0.650

The ROC curves for all four classifiers are shown in Figure 2 illustrating their ability to discriminate between agglomeration and rebound events across all decision thresholds. The RF model achieves the highest overall performance, consistently maintaining superior true positive rates across a wide range of false positive rates. The SVM-RFB and LR models show similar overall performance outperforming the RF at low decision thresholds (FPR<0.1). The moderate performance of the LR suggest that the engineered feature space is partially linearly separable. The MLP model exhibits the weakest overall performance across all thresholds indicating the chosen architecture and small dataset is insufficient to learn from.

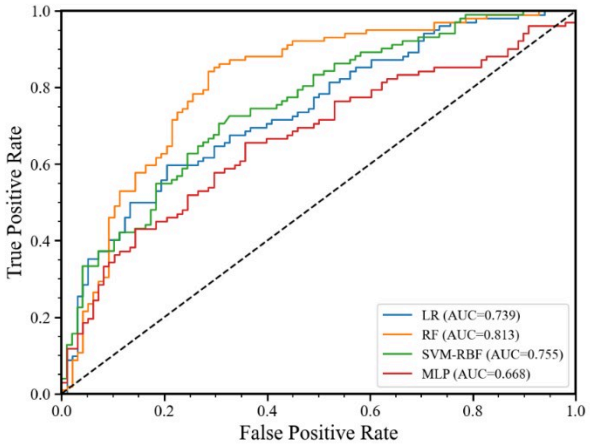

Figure 2: Receiver operating characteristic curves for the four machine learning models used to predict binary collision outcomes. The diagonal dashed line represents random classification performance. The area under the curve is reported in the legend for each model.

3.3 Feature Importance

To gain understanding of the physical mechanisms driving collision outcomes permutation importance was conducted on the RF model. This model was chosen since it demonstrated the highest predictive accuracy and robustness. This technique quantifies the relative contribution of each engineered feature by measuring the decrease in model performance when the feature's values are randomly permuted.

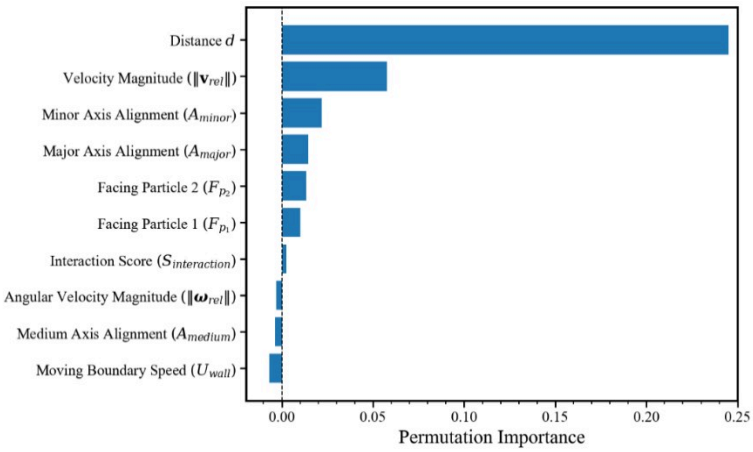

Figure 3: Ranked permutation importance of engineered features for the RF model. Higher values indicate a greater reliance on the feature for predicting collision outcomes.

Figure 3 shows that collision outcome is primarily governed by the separation distance and the relative linear velocity magnitude . The distance parameter , constrained by where and are the semi-minor and semi-major axes of the ellipsoid, acts as a compact representation of collision geometry. Smaller values of correspond to face-to-face interactions with larger contact areas that favour energy dissipation and DLVO agglomeration, whereas larger values indicate tip-to-tip contacts that are more likely to rebound. The strong importance of reflects the role of translational kinetic energy in determining whether sufficient energy can be dissipated for agglomeration to occur.

Secondary contributions arise from the geometric alignment features and , which refine the contact description for collisions with similar separation distances but different rotational configurations. In contrast, the facing metrics , , interaction score , angular velocity magnitude , medium-axis alignment ,

and wall velocity showed comparatively low or negative importance, indicating that these features contribute little additional predictive information beyond that already captured by and .

4. Conclusions

This study developed a machine learning framework to predict binary collision outcomes between non-spherical ellipsoidal particles as either agglomerating or bouncing. Four classifiers were tested using collision features from turbulent channel flow simulations, with the random forest model performing best (ROC-AUC = 0.813, F1 = 0.759). Results showed that nonlinear feature interactions strongly influence collision outcome. Permutation importance analysis identified inter-centroid distance and relative linear velocity as the most important predictors, while geometric alignment features had smaller effects. Angular velocity, medium-axis alignment, and wall velocity contributed little. Overall, the framework accurately predicts collision outcomes using a compact, physically interpretable feature set.

5. Acknowledgements

The authors would like to thank the EPSRC (EP/S022732/1) and Sellafield Ltd for funding.

6. References

1. L. Brandt and F. Coletti (2022). Particle-laden turbulence: Progress and perspectives, Ann. Rev. Fluid Mech., 54:159-189.

2. N. Paul, S. Biggs, M. Edmondson, T. N. Hunter and R. B. Hammond (2013). Characterising highly active nuclear waste simulants, Chem. Eng. Res. Des., 91:742-751.

3. J. Eaton and J. Fessler (1994). Preferential concentration of particles by turbulence, Int. J. Multiph. Flow, 20:169-209.

4. C. Marchioli, A. Soldati, J.G.M. Kuerten, B. Arcen, A. Taniere, G. Goldensoph, K.D. Squires, M.F. Cargnelutti and L. Portela (2008). Statistics of particle dispersion in direct numerical simulations of wall-bounded turbulence, Int. J. Multiph. Flow, 34:879-893.

5. B. van Wachem, M. Zastawny, F. Zhao and G. Mallouppas (2015). Modelling of gas-solid turbulent channel flow with non-spherical particles with large Stokes numbers, Int. J. Multiph. Flow, 68:80-92.

6. C. Marchioli, M. Fantoni and A. Soldati (2010). Orientation, distribution, and deposition of elongated inertial fibers in turbulent channel flow, Phys. Fluids, 22:033301.

7. C. Peskin (2002). The immersed boundary method, Acta Numer., 11:479-517.

8. J.P. Anderson, L.F. Mortimer, T.N. Hunter, J. Peakall and M. Fairweather (2025). Numerical simulation of the agglomeration behaviour of spheroidal particle pairs in chaotic flows, Flow Turbul. Combust., 114:941-965.

9. M. Breuer and N. Almohammed (2015). Modeling and simulation of particle agglomeration in turbulent flows using a hard-sphere model with deterministic collision detection, Int. J. Multiph. Flow, 73:92-111.

10. L.F. Mortimer, D.O. Njobuenwu and M. Fairweather (2020). Agglomeration dynamics in liquid-solid particle-laden turbulent channel flows using an energy-based deterministic approach, Phys. Fluids, 32:063302.

11. B. Derjaguin and L. Landau (1941). Theory of the stability of strongly charged lyophobic sols, Acta Physicochim. URSS, 14:633-662.

12. E.J.W. Verwey and J.T.G. Overbeek (1948). Theory of the Stability of Lyophobic Colloids, Elsevier, Amsterdam.

13. L.F. Mortimer and M. Fairweather (2021). Assessment of behavioral modification techniques through immersed boundary method simulation of binary particle interactions in isotropic turbulence, Phys. Fluids, 33:053309.

14. L.F. Mortimer and M. Fairweather (2025). A hybrid machine-learning algorithm for predicting particle trajectories and dynamics in wall-bounded turbulent flows, Chem. Eng. Technol., 48:e70215.

15. L. Fischer, J. W. Lottes, S. G. Kerkemeier, “Nek5000”, Argonne National Laboratory, 2008, http://nek5000.mcs.anl.gov

Proceedings of the 2nd International Symposium on AI and Fluid Mechanics
Paper No [leave blank]

A Neural Surrogate Model for Predicting Drop-Impact Spreading and Force Responses

Zikai Zhang; Emil Sardaryan; David L. S. Hung*;

Global College, Shanghai Jiao Tong University, China;

Abstract

Predicting drop impact response based on a limited number of experiments is challenging because spreading and impact force evolve on different time scales and are affected by run-to-run variability. This study develops an experimental response surrogate for water drops impacting on a solid surface. High-speed side-view imaging and synchronized force sensing are used to obtain spreading and force response from 48 runs covering 16 impact conditions, covering initial droplet diameters from 2.86 to 3.60 mm and impact velocities from 1.40 to 2.80 m/s. The measurements show that increasing impact velocity and drop size leads to larger spreading and higher peak force, while the force response is concentrated in the early impact stage (0-2 ms) and the geometric response evolves over a longer time (0-12 ms). A multi-output neural network is trained to map nondimensional time and impact-condition variables to the measured response curves. Condition-level cross-validation shows that the model predicts impact conditions with a mean spreading-factor rRMSE of 6.05% and a mean impact force rRMSE of 13.59%, indicating the proposed model can provides accurate time-resolved predictions of both spreading and force responses over the tested range of droplet sizes and impact velocities.

Keywords: Drop impact; neural surrogate; response prediction

1. Introduction

Drop impact on solid surfaces is a representative transient multiphase-flow problem in which interface deformation, contact-line motion and force transmission occur over millimetric length scales and millisecond time scales. It appears in spray cooling, coating, inkjet printing, erosion, anti-icing and the design of water-repellent surfaces. Previous studies have described drop impact through reduced observables and scaling laws. Reviews by Yarin and by Josserand and Thoroddsen give the broader picture of spreading, splashing, recoiling and bouncing [1,2]. Rioboo et al. showed how dry-surface impact depends on wettability, surface condition and dimensionless groups such as Re, We and Oh [3]. More recent work has tied deformation and force more closely together. For instance, Sanjay and Lohse proposed a unifying scaling theory for impact force and maximum spreading diameter, arguing that these two responses should be treated within the same physical picture [4]. Zhang et al. measured water-drop impact forces on superhydrophobic surfaces and showed that rebound and non-wetting contact can produce multiple force peaks [5]. These studies show that spreading and force are coupled signatures of the same impact process. However, scaling laws usually target extrema, characteristic times or dominant trends, and do not directly provide continuous curve prediction for new combinations of drop size and impact velocity.

Machine learning provides a practical route for learning such condition-dependent response maps in fluid mechanics [6]. Related developments in physics-informed and scientific machine learning have shown how neural models can be adapted to physical systems, while also revealing sensitivity to loss construction and optimization [7-10]. In this study, we construct an experimental response surrogate based on a multi-output neural network. The model maps nondimensional time and impact-condition variables to the spreading factor and impact force, and is evaluated by complete-condition cross-validation to test prediction for drop diameters and release heights.

2. Method

The experiments consist of water drops released from prescribed heights and impacting a horizontal solid substrate instrumented for force measurement. A side-view high-speed camera records the drop profile during impact at 5000 fps, while an oscilloscope records the calibrated force signal from the substrate sensor. The present data set contains 48 runs grouped into 16 impact conditions, with three repeated runs for

each condition. The conditions are defined by four release heights and four needles shown in table 1, giving initial diameters from approximately 2.86 to 3.60 mm and impact velocities from approximately 1.40 to 2.80 m/s. The side-view image sequence provides 60 contour frames per run over a 0-12 ms window. The force signal is baseline corrected, low-pass filtered at 5 kHz, and converted to force using the calibrated voltage-to-force factor. The overall experimental workflow and the corresponding neural-network architecture are summarized in figure 1.

Table 1. Needle series used to generate drops in experiment and their corresponding drop diameters.

Needle gauge series	G18	G20	G22	G24
Drop diameter (mm)	3.60	3.29	3.10	2.86

From each contour frame, the outlines of drop are extracted. The spreading factor is defined as , where is measured from the outlines as the wetted diameter. The impact force is nondimensionalized as , where is the impact force measured by sensor. Time is written as . Each run is kept as an independent realization during training; repeated runs are not averaged before fitting. This preserves run-to-run variability while allowing condition-level statistics to be computed later.

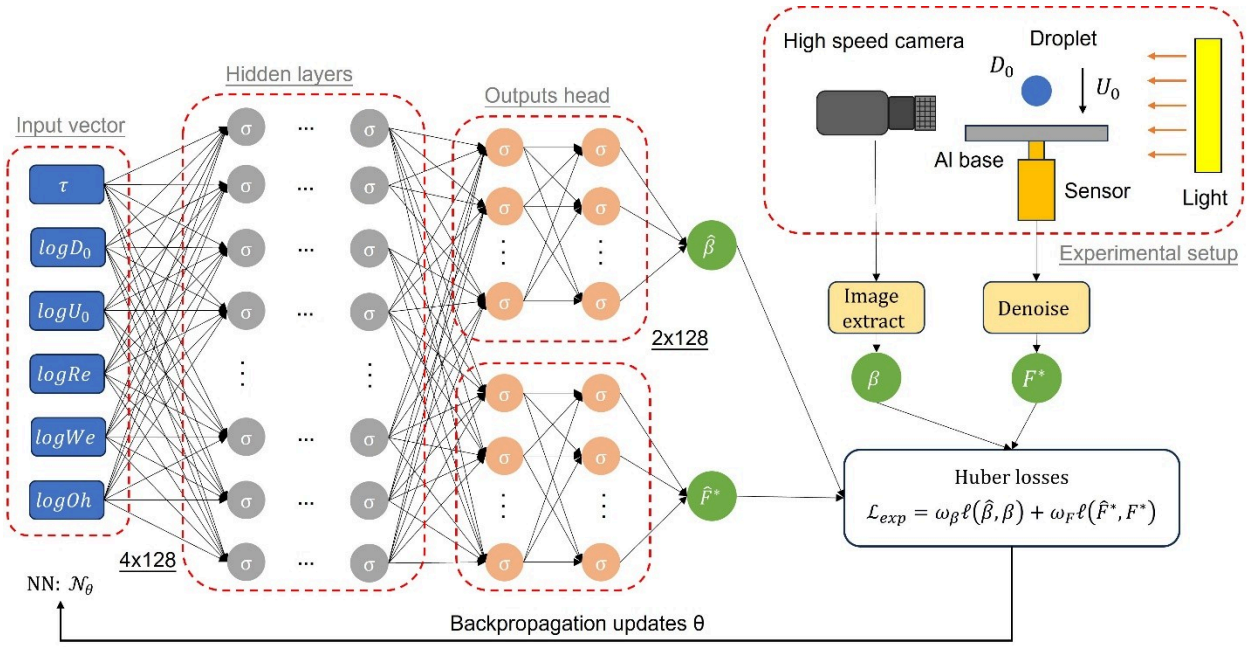

Figure 1. Experimental response surrogate for drop-impact response prediction.

The experimental response surrogate is implemented as a multi-output neural network that maps nondimensional time and impact condition to the measured response curves. The input vector contains Fourier features of and standardized logarithm of the condition variables: initial diameter , initial velocity , Reynolds number , Weber number , and Ohnesorge number . The model has a shared multilayer perceptron trunk followed by two heads: a geometry head for and a force head for . In compact form,

where denotes the sinusoidal time encoding. In the implementation used here, the trunk width is 128, the trunk has four hidden layers, each head has two hidden layers, and the activation function is SiLU. The geometry outputs are passed through a softplus transform to keep them positive.

The network is trained using measured response data. Geometry and force samples are drawn in separate batches so that the much denser force trace does not dominate the contour data. Sampling is balanced at the case level. The loss is a weighted sum of Huber losses, with a lower weight assigned to spreading than to force where in the default configuration. The force term is assigned a larger weight because is a short-duration transient with steeper temporal gradients, whereas evolves more smoothly over the impact window. Model performance is evaluated by holding out complete impact conditions, so that all repeated runs from a validation condition are excluded from training.

3. Results

Figure 2 summarizes the experimentally observed spreading and force response during drop impact. Figure 2(a) shows representative side-view image sequences for G18 and G24 drops. Before impact, the G18 drop has a larger initial diameter than the G24 drop, consistent with the needle-calibrated diameters of 3.60 mm and 2.86 mm, respectively. After contact, both drops undergo rapid radial expansion driven by the incoming

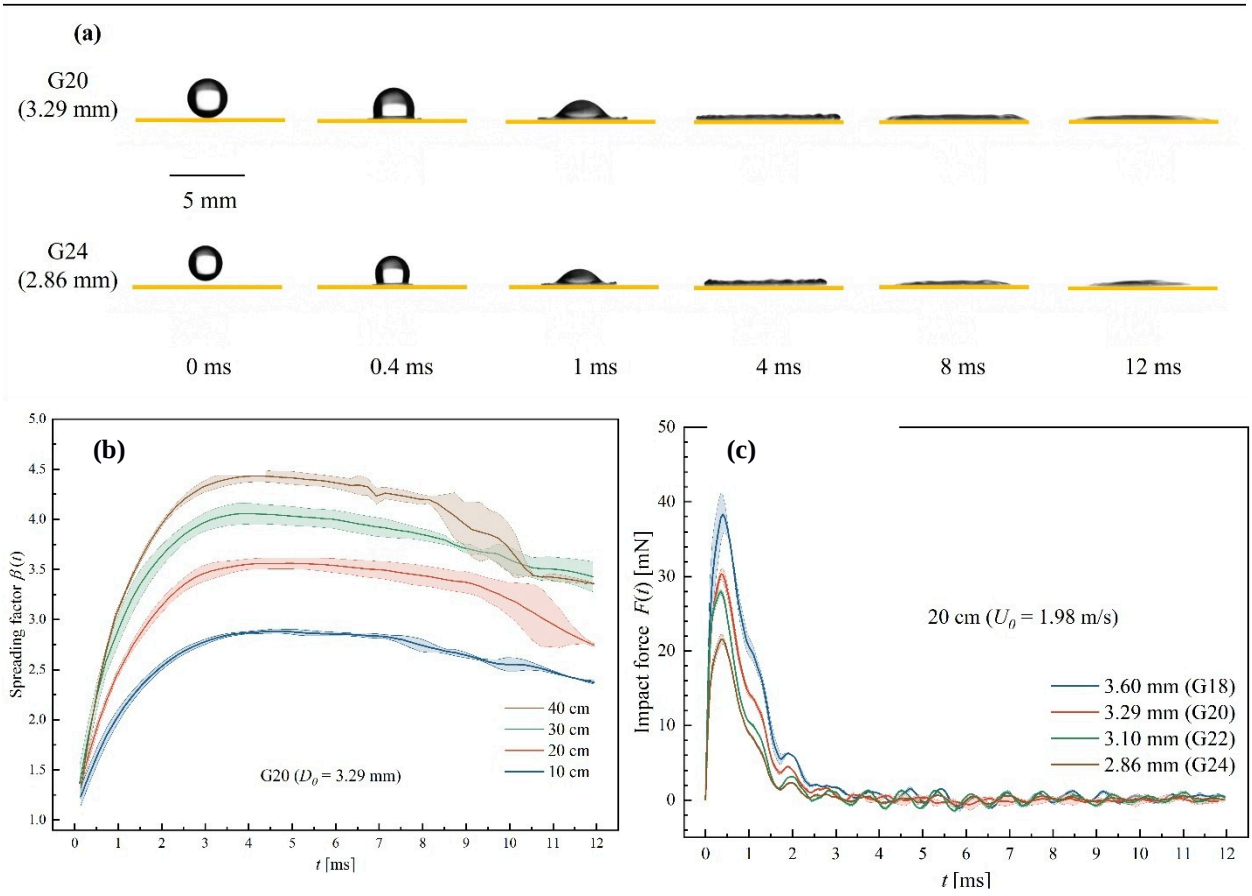

Figure 2. Experimental characterization of drop spreading and impact force. (a) Representative side-view image sequences comparing G20 and G24 drops under the same release height of 20 cm. (b) Time evolution of the spreading factor β, for G20 drops under different release heights. (c) Force response at a fixed release height of 20 cm for different drop sizes produced by 4 different needles. All curves are averaged over three repeated experiments, with error bars denoting one standard deviation.

inertia. During the early spreading stage from 0 to 1 ms, the liquid rim rises around the spreading lamella and forms a crown-like shape near the contact region. As the lamella continues to expand, the drop becomes progressively flatter. After 4 ms, the profile grows into a thin, flattened shape, and the subsequent motion is dominated by slower spreading and weak retraction. The present analysis focuses on the early impact process within a 0-12 ms time window; within this interval, no clear recoil into a compact secondary drop is observed. Comparing the two cases, the larger G18 drop maintains a visibly larger spreading diameter throughout the impact process, whereas the G24 drop forms a smaller lamella under the same release condition.

The spreading factor and impact force provide complementary descriptions of the same impact event: the former characterizes the geometric evolution of the drop, whereas the latter captures the short-time contact response measured by the sensor. Figure 2(b)&(c) shows the characterization of drop spreading and impact force under different conditions. For G20 drops, increasing the release height leads to faster impact and larger spreading rate. The mean maximum spreading factor increases from approximately 2.89 at 10 cm to 4.43 at 40 cm around 4 ms. At the fixed release height of 20 cm, increasing the drop size from G24 to G18 increases the mean peak force from 21.6 mN to 38.5 mN. And all the peak forces appear around 0.5 ms, not influenced by diameter difference.

The two measured responses also evolve on different time scales. The force response is concentrated in the early stage of impact: most cases exhibit a rapid rise to a dominant peak within the first 0-1 ms, followed by a fast decay toward the baseline. In contrast, the spreading factor evolves over the longer spreading and reduction period within the whole 12 ms time window, first increasing as the lamella expands and then decreasing or stabilizing depending on the impact condition.

An experimental response surrogate was trained to predict the spreading factor and impact force from nondimensional time and impact-condition variables. To evaluate whether the model learned a condition-level response map rather than repeated-run or time-point correlations, the 16 experimental conditions were arranged as a 4×4 grid defined by release height and needle gauge. A balanced cross-validation split was used. Each fold held out four complete impact conditions, with one condition selected from each release height and one condition selected from each needle gauge. All three repeated runs of each held-out condition were kept in the validation set. This split prevents leakage between repeated experiments and avoids validation sets biased toward only one velocity or drop-size range.

Representative predictions are shown in Figure 3 for two validation cases, 20 cm/G20 and 30 cm/G24. These two cases sample different regions of the experimental grid: the former corresponds to an intermediate drop size and impact velocity, while the latter corresponds to a smaller drop at a higher impact velocity. In both cases, the model reproduces the main temporal trend of the response. The predicted spreading factor follows the rapid initial growth, the approach to maximum spreading and the subsequent slow reduction. The force prediction also captures the temporal evolution trend, including the rapid rise and decay that occur much earlier than the maximum spreading time. This agreement indicates that the surrogate is not only fitting scalar extrema, but learning the different time scales of the geometric and force responses.

The condition-wise prediction errors are summarized in Table 2. Each table entry reports the paired β rRMSE and F rRMSE for one validation impact condition. The spreading-factor errors are generally lower than the force errors, which is consistent with the different temporal character of the two signals. The reason is that the spreading factor evolves smoothly over the 0-12 ms window and is therefore less sensitive to small time shifts. In contrast, the force response is transient and concentrated near the initial contact stage around 0-2 ms. Small errors in impact-time alignment or early contact dynamics can therefore produce larger errors in F(t). This explains why the force rRMSE is systematically higher than the β rRMSE, even when the predicted force curve captures the main rise-and-decay trend.

The error distribution also reflects the trend of the experimental condition space. For β(t), the largest errors appear mainly at higher release heights, where larger spreading rate and later-stage reduction make the spreading curve more difficult to match. For F(t), the larger rRMSE values are consistent with the transient nature of the impact-force signal. Because the force signal changes very rapidly, a small shift in the predicted peak time can lead to a relatively large error, even when the overall force curve shape is well reproduced. These results indicate that the surrogate captures the main response trends across drop size and impact velocity, while the remaining errors are concentrated in the short-time force dynamics and in strongly deforming spreading cases.

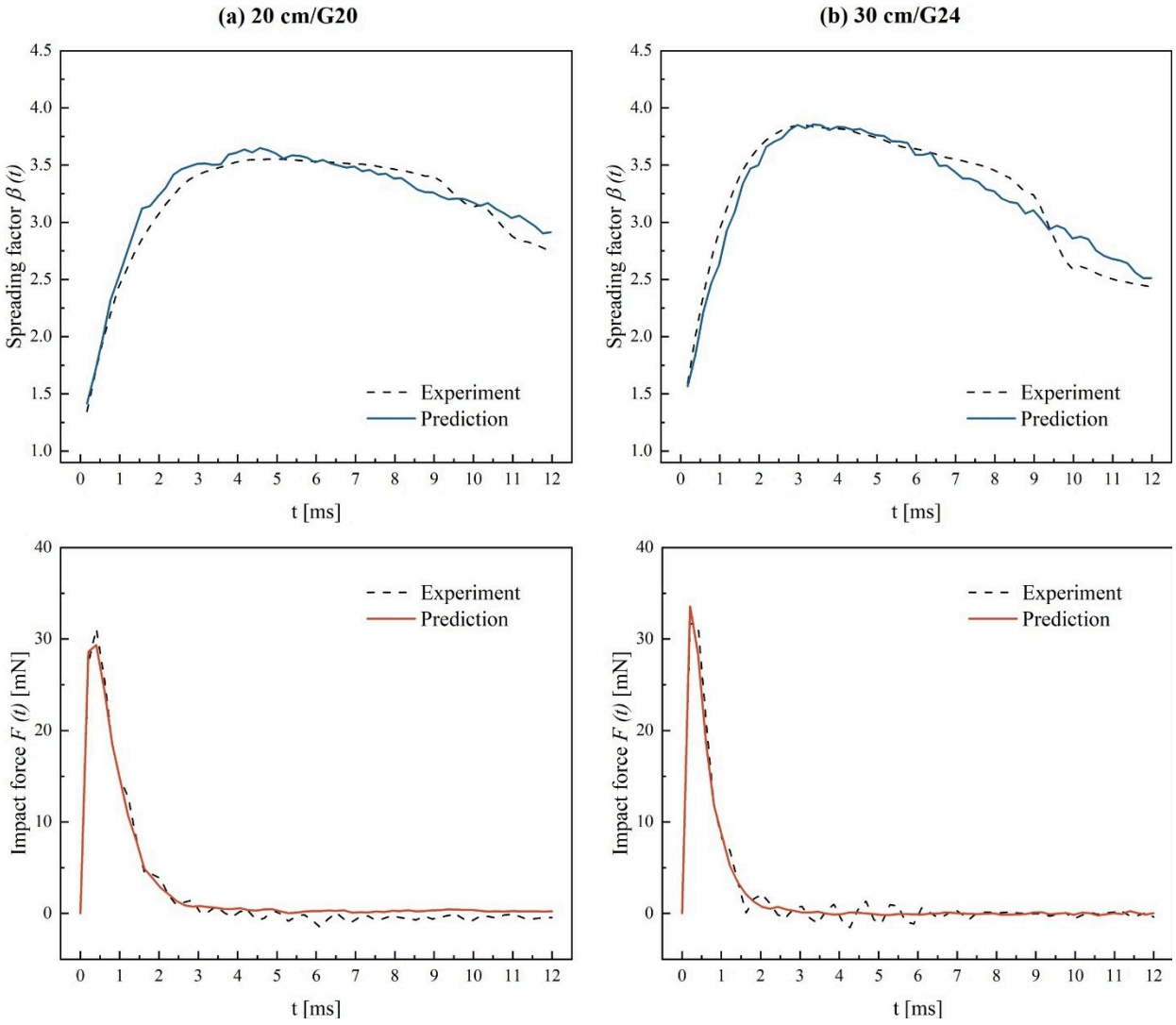

Table 2. Condition-wise prediction errors of the experimental response surrogate.

Figure 3. Prediction of spreading factor and impact force for representative drop impact conditions. (a) 20 cm/G20. (b) 30 cm/G24. The upper panels compare the measured and predicted spreading factor β(t), while the lower panels show the corresponding impact force F(t).

G18	7.13	13.37	6.10	12.48	6.44	17.16	9.54	15.41

G20	1.93	8.38	3.75	9.73	6.56	13.33	8.41	16.15
G22	2.43	12.88	4.73	12.78	7.34	12.34	8.84	12.62
G24	3.76	17.09	6.85	17.83	3.94	12.01	9.01	13.75

4. Conclusion & Future Work

This study developed an experimental response surrogate for drop impact prediction using synchronized high-speed imaging and force measurements. The main contribution is to connect directly measured spreading and force histories with a condition-level neural prediction framework. Instead of only focusing on maximum spreading or peak force for each impact event, the proposed multi-output network learns time-resolved response curves from nondimensional time and impact-condition variables. Condition-level cross-validation shows that the proposed surrogate can precisely predict all the impact conditions, preserving the main spreading evolution and early-stage force peak.

The present work serves as an initial step toward more comprehensive neural modelling of drop impact. The current model predicts scalar response, including spreading factor and impact force, rather than the full interface evolution. In future work, the network architecture will be extended toward complete drop-shape prediction so that the temporal evolution of the interface can be represented more directly. The experimental scope will also be broadened to include impacts on surfaces with different wettability and geometry, to cover a wider range of spreading, recoiling and rebound behaviors.

References

1. A. L. Yarin (2006). ‘Drop impact dynamics: splashing, spreading, receding, bouncing...’, Annual Review of Fluid Mechanics, 38, 159-192. DOI: 10.1146/annurev.fluid.38.050304.092144.
2. C. Josserand and S. T. Thoroddsen (2016). ‘Drop impact on a solid surface’, Annual Review of Fluid Mechanics, 48, 365-391. DOI: 10.1146/annurev-fluid-122414-034401.
3. R. Rioboo, M. Marengo and C. Tropea (2002). ‘Time evolution of liquid drop impact onto solid, dry surfaces’, Experiments in Fluids, 33(1), 112-124. DOI: 10.1007/s00348-002-0431-x.
4. V. Sanjay and D. Lohse (2025). ‘Unifying Theory of Scaling in Drop Impact: Forces and Maximum Spreading Diameter’, Physical Review Letters, 134, 104003. DOI: 10.1103/PhysRevLett.134.104003.
5. B. Zhang, V. Sanjay, S. Shi, Y. Zhao, C. Lv, X.-Q. Feng and D. Lohse (2022). ‘Impact Forces of Water Drops Falling on Superhydrophobic Surfaces’, Physical Review Letters, 129, 104501. DOI: 10.1103/PhysRevLett.129.104501.
6. S. L. Brunton, B. R. Noack and P. Koumoutsakos (2020). ‘Machine learning for fluid mechanics’, Annual Review of Fluid Mechanics, 52, 477-508. DOI: 10.1146/annurev-fluid-010719-060214.
7. M. Raissi, P. Perdikaris and G. E. Karniadakis (2019). ‘Physics-informed neural networks: a deep learning framework for solving forward and inverse problems involving nonlinear partial differential equations’, Journal of Computational Physics, 378, 686-707. DOI: 10.1016/j.jcp.2018.10.045.
8. G. E. Karniadakis, I. G. Kevrekidis, L. Lu, P. Perdikaris, S. Wang and L. Yang (2021). ‘Physics-informed machine learning’, Nature Reviews Physics, 3, 422-440. DOI: 10.1038/s42254-021-00314-5.
9. J. Willard, X. Jia, S. Xu, M. Steinbach and V. Kumar (2023). ‘Integrating scientific knowledge with machine learning for engineering and environmental systems’, ACM Computing Surveys, 55(4), Article 66, 1-37. DOI: 10.1145/3514228.
10. S. Wang, Y. Teng and P. Perdikaris (2021). ‘Understanding and mitigating gradient flow pathologies in physics-informed neural networks’, SIAM Journal on Scientific Computing, 43(5), A3055-A3081. DOI: 10.1137/20M1318043.

Prediction of Turbophoretic Particle Transport in Wall-Bounded Turbulent Flows Using Long Short-Term Memory Neural Networks

[1]Lee Mortimer*; [1]Michael Fairweather

[1]*School of Chemical and Process Engineering, University of Leeds, Woodhouse Lane, Leeds, LS2 9JT, UK*

Keywords: Machine learning; Particle-laden flows; Turbulence; Turbophoresis; Digital twins

Abstract. Turbophoresis presents a major challenge for digital-twin modelling of particle-laden turbulent flows, as near-wall particle accumulation arises from particle-fluid interactions which are difficult to capture without computationally intensive direct numerical simulations (DNS) coupled with Lagrangian particle tracking (LPT). At present, this limits the development and implementation of near real-time digital twins in applications where inertial particle transport is critical such as in the processing of nuclear waste. In this work, a long short-term memory (LSTM) neural network is developed alongside a hybrid ML simulation framework to predict turbophoretic particle dynamics in turbulent channel flows. The model is trained on a large database of high-fidelity DNS-LPT data and learns the temporal correlations governing particle-turbulence interactions using sequences of particle position and velocity histories. The LSTM is evaluated across two Stokes numbers which consider weak and moderate inertial response times, allowing for assessment of its ability to reproduce turbophoresis-driven migration and near-wall accumulation. For low Stokes numbers, the model accurately reproduces mean velocities, velocity fluctuations, and near-uniform concentration profiles without introducing fake turbophoretic drift as in previous methods. At intermediate Stokes numbers, the LSTM captures the onset and increase in turbophoretic migration magnitude, recovering near-wall accumulation trends consistent with DNS-LPT. The study analyses the model's ability to recover first- and second-order particle statistics, wall-normal concentration profiles and assesses limitations of the technique. These results demonstrate progress toward temporal history-based machine learning models suitable for digital-twin frameworks for inertial particle transport in wall-bounded turbulence.

1. Introduction

Machine learning (ML) has rapidly become an important computational tool for analysis, prediction and decision-making across both science and industry, with applications ranging from healthcare [1] to autonomous vehicles [2], among many others. Its scientific value lies in its ability to construct data-driven models which improve as more information becomes available. In fluid dynamics, ML is increasingly being used for turbulence modelling, flow reconstruction and flow optimisation [3, 4]. These methods commonly use high-fidelity simulations or experimental measurements to train predictive models that can improve accuracy while reducing computational cost. Over the past decade, ML-based approaches have shown considerable promise in recovering fluid-flow fields, identifying turbulent-flow features and accelerating simulations for industrially relevant applications [5]. Multiphase flows, and particle-laden turbulent flows in particular, remain a more challenging problem. Particle motion is influenced by turbulent fluctuations, inertia-driven effects, turbophoresis, preferential accumulation and particle-flow coupling, with these effects becoming increasingly complex and difficult to predict at increased concentrations and Stokes numbers [6, 7]. Previous hybrid ML studies of turbulent dispersed flows have shown that data-driven models are able to reproduce important first- and second-order statistics at substantially lower cost than fully resolved simulations [8-10]. However, maintaining predictive accuracy across dynamic flow and particle conditions remains a key challenge. This is particularly true for particle concentration fields, which are often omitted from the assessment of such models despite being essential for practical prediction and design [11]. Addressing this limitation is necessary if ML-based methods are to move beyond case-specific regression and become reliable predictive tools and form an important milestone in the feasibility of digital twin technologies.

In this study, we develop and assess a predictive framework based on long short-term memory (LSTM) networks trained using databases generated by direct numerical simulation (DNS) coupled with Lagrangian particle tracking (LPT). The model is trained using DNS-LPT trajectory data at $Re_\tau = 180$,

covering a broad range of particle diameters and density ratios relevant to practical dispersed-flow systems. By modelling temporal dependencies and correlations directly, LSTMs are well suited to capturing the long-range, non-Markovian behaviour associated with particle-turbulence interactions [4]. They are therefore used here to learn the temporal evolution of particle trajectories in turbulent channel flow. The present work further extends previous approaches by introducing a conditional generative modelling framework for particle-laden turbulent channel flows. Rather than using ML solely to predict the next particle state from its current state or recent history, the new method aims to learn a probabilistic representation of trajectory evolution conditioned on both the carrier-flow conditions and the particle properties. Trajectory segments extracted from DNS-LPT databases are used to train a conditional generative model in which the Reynolds number, particle diameter, density ratio and initial particle state are supplied as conditioning variables. A latent stochastic variable is also included to represent the variability between trajectories that evolve under the same macroscopic conditions. The model is assessed through its ability to reproduce statistical behaviour across a range of Stokes numbers. This includes not only low-order quantities, but also the qualitative structure and temporal coherence of Lagrangian particle trajectories over extended periods. This is a more demanding objective than matching mean quantities alone, since realistic particle paths depend on persistence, temporal correlations and repeated interactions with turbulent structures in the carrier flow. These capabilities support the development of LSTM-based conditional generative hybrid ML models as potential components of digital-twin technologies, where pre-trained surrogate models may enable near-real-time simulation, prediction and control.

2. Methodology

2.1 DNS/LPT database

The carrier-phase turbulent channel flow was generated using direct numerical simulation through use of the open-source spectral element-based solver, Nek5000 [12]. The simulations considered a statistically stationary turbulent channel flow at a shear Reynolds number of $Re_\tau = 180$. The computational domain was $4\pi h \times 2h \times 2\pi h$ in the streamwise, wall-normal and spanwise directions, respectively, where h is the channel half-height. The spectral element mesh contained approximately 3.9 million Gauss-Lobatto-Legendre nodes, with refinement in the wall-normal direction to resolve near-wall turbulence structures. Periodic boundary conditions were applied in the streamwise and spanwise directions, while no-slip and impermeability conditions were imposed at the channel walls, $y = \pm h$. The flow was driven by a constant pressure gradient and advanced using a fixed non-dimensional timestep of $\Delta t^* = 0.005$. All spatial and temporal variables were non-dimensionalised using bulk-flow properties. Henceforth, any property with an asterisk (*) indicates a variable non-dimensionalised in this way. The dispersed phase was modelled using an in-situ Lagrangian particle tracker. Particles were treated as point-like, impenetrable spheres and were advanced concurrently with the DNS. After each fluid timestep, the required carrier-phase quantities were spectrally interpolated to each particle location. The particle force balance was integrated using a fourth-order Runge-Kutta scheme with the same timestep as the fluid solver. The force terms considered were drag, lift, virtual mass and pressure-gradient contributions. Particle-wall collisions were treated as perfectly elastic, such that the wall-normal particle velocity component was reversed after impact. Periodicity was applied to particle positions in the streamwise and spanwise directions. Particle data were written every 10 fluid timesteps, corresponding to a saved interval of $\Delta t_S^* = 0.05$. Each instantaneous file contained 10,000 particles and stored the particle positions and instantaneous velocity components. The DNS-LPT database therefore consisted of the following particle trajectory records:

$$\left[x^*,\ y^*,\ z^*,\ v_x^*,\ v_y^*,\ v_z^*\right]_{i,t}, \tag{1}$$

where i is the particle index and n is the saved timestep. These variables were stored with the associated simulation labels, c:

$$c = [Re_\tau,\ d_p^*,\ \rho_P^*], \tag{2}$$

where d_p^* is the particle diameter to the channel half-height ratio and ρ_P^* is the particle-to-fluid density ratio. These labels were subsequently used as conditioning variables for the machine-learning model.

2.2 Conditional generative LSTM and hybrid ML framework

The DNS-LPT instantaneous data were first reorganised into Lagrangian trajectory sequences by linking each particle across consecutive saved snapshots. Overlapping trajectory windows of fixed length $N_{WIN} = 20$ were then extracted from the full particle histories. Each sequence retained the wall-normal particle position and the three particle velocity components,

$$s_P^n = [y_P^n, u_P^n, v_P^n, w_P^n], \tag{3}$$

together with the corresponding simulation parameters $Re_\tau,\ d_p^*,\ \rho_P^*$. The initial particle state at the start of each window was also retained explicitly, allowing generated trajectories to be started from physically admissible initial conditions. All variables were normalised using statistics from the training subset, and the data were divided into training, validation and test sets using a 70:20:10 split. The hybrid ML model was formulated as a conditional generative sequence model based on a variational autoencoder-type architecture with long short-term memory layers. The LSTM structure was used because inertial particle motion in turbulence is history-dependent: the particle response depends on its current state, recent velocity history and accumulated momentum. The generative formulation allowed multiple plausible trajectory realisations to be produced for the same macroscopic flow and particle conditions, rather than a single deterministic path. The model consisted of an encoder and a decoder. During training, the encoder received a DNS-LPT trajectory window and used LSTM layers to extract its temporal structure. The encoded representation was projected into a latent space described by a mean and log-variance, from which a latent vector $\boldsymbol{z}$ was sampled using the standard variational reparameterisation procedure. The decoder then reconstructed the trajectory window using the sampled latent vector and the conditioning information. The learned conditional mapping may be written as,

$$(\boldsymbol{c}, \boldsymbol{s}_0, \boldsymbol{z}) \longrightarrow \left[y^*(t), v_x^*(t), v_y^*(t), v_z^*(t)\right]_{t=1}^{T}, \tag{4}$$

where $\boldsymbol{z}$ is the sampled latent vector and $\boldsymbol{s}_0$ is the initial particle state. The conditioning variables therefore define both the governing flow/particle parameters and the starting state of the generated trajectory. Training was based on both trajectory reconstruction and agreement with DNS-LPT particle phase statistics. The total loss combined a reconstruction term, a Kullback-Leibler divergence term for latent-space regularisation, and statistical penalties on the wall-normal concentration profile, the mean particle velocity profiles and the RMS particle velocity fluctuation profiles. The loss was calculated as,

$$\mathcal{L}_T = \mathcal{L}_\mathrm{r} + \beta\mathcal{L}_\mathrm{KL} + \lambda_\phi\mathcal{L}_\phi + \lambda_u\mathcal{L}_u + \lambda_{u'}\mathcal{L}_{u'}, \tag{5}$$

where $\mathcal{L}_\mathrm{r}$ penalises differences between generated and DNS-LPT trajectory windows, $\mathcal{L}_\mathrm{KL}$ regularises the latent distribution, $\mathcal{L}_\phi$ constrains the wall-normal particle concentration, $\mathcal{L}_u$ constrains the mean velocity profiles and $\mathcal{L}_{u'}$ constrains the RMS velocity fluctuation profiles. The terms β, λ_ϕ, λ_u and $\lambda_{u'}$ are weighting coefficients which control the relative influence of latent regularisation and statistical matching. The weighting coefficients were set to $\beta = 10^{-4}$, $\lambda_\phi = 1$, $\lambda_u = 1$ and $\lambda_{u'} = 1$, with equal weighting also applied to the reconstruction terms for y^*, v_x^*, v_y^* and v_z^*. This combined objective was used so that the model reproduced both individual trajectory segments and the first- and second-order dispersed-phase statistics. Once trained, the decoder was used to generate synthetic particle trajectories for prescribed $Re_\tau,\ d_p^*,\ \rho_P^*$ and initial particle state. A latent vector was sampled from the learned distribution and passed to the decoder with the conditioning variables. During generation, reflective wall

treatment was applied to prevent wall penetration and to remain consistent with the DNS-LPT calculations. If a generated wall-normal position crossed $y^* = \pm 1$, the particle was reflected back into the channel as an elastic rebound. Periodic behaviour was imposed in the streamwise and spanwise directions. Repeated latent sampling therefore produced synthetic particle ensembles analogous to DNS-LPT datasets, but at substantially reduced computational cost.

3. Results and discussion

The performance of the conditional generative LSTM-based hybrid ML model is assessed by comparing DNS-LPT results with generated particle statistics and trajectories for two representative particle response regimes. The first is at $St^+ = 0.03$, representing a very low Stokes-number case in which particles respond almost instantaneously to the carrier-phase turbulence. The second corresponds to $St^+ = 23$, representing an intermediate-Stokes-number case in which particle inertia becomes significant and the dispersed phase exhibits a finite response time. In previous studies, it is widely known that preferential concentration behaviour is expected to be weak for the low-Stokes-number particles, which remain closely coupled to the fluid, but increased for the intermediate-Stokes-number particles, which migrate via turbophoresis down gradients of turbulence intensity and preferentially accumulate near the wall.

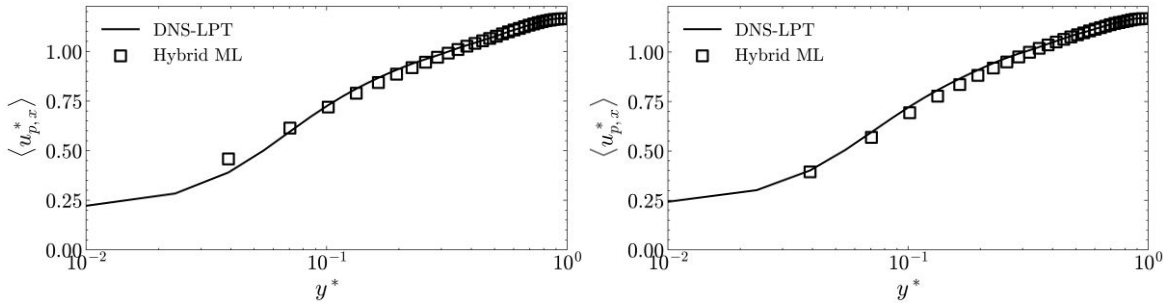

Figure 1: Mean streamwise particle velocity, comparing DNS-LPT against the LSTM hybrid model predictions. Left: $St^+ = 0.03$, right: $St^+ = 23$.

Figure 1 compares the mean streamwise particle velocity profiles for the low- and intermediate-Stokes-number cases. For $St^+ = 0.03$, the particles behave almost as tracers and closely follow the local carrier-phase velocity, leading to a smooth mean velocity profile which is reproduced well by the model, other than a slight overprediction very close to the wall. For $St^+ = 23$, the particles possess sufficient inertia for their motion to decouple partly from the local fluid velocity. The ML model captures the main increase in mean streamwise velocity from the near-wall region to the channel centre, indicating that it preserves the dominant wall-normal structure of particle advection. Any deviations close to the wall are physically important because this is the region where turbophoretic drift, wall-normal turbulent transport and elastic wall interactions all contribute to local particle velocity statistics.

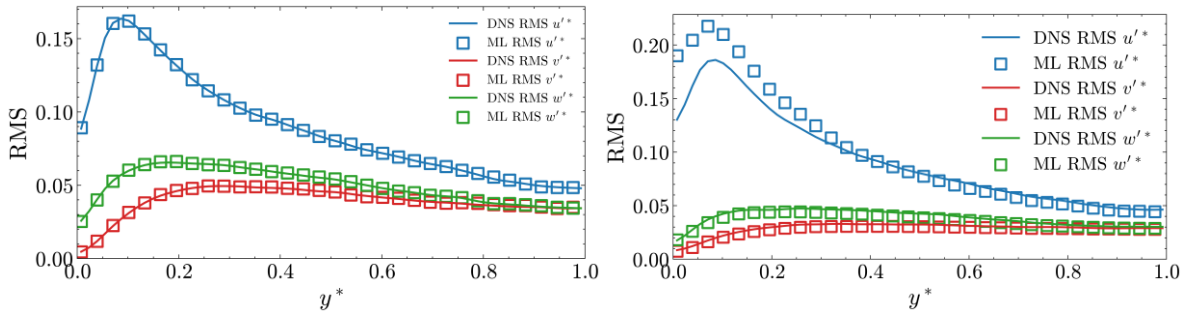

Figure 2: RMS of particle velocity fluctuations, comparing DNS-LPT against the LSTM hybrid model predictions. Left: $St^+ = 0.03$, right: $St^+ = 23$.

Figure 2 compares the RMS particle velocity fluctuations for $St^+ = 0.03$ and $St^+ = 23$. For the low-Stokes-number case, the particles respond rapidly to the surrounding turbulent eddies, so their velocity fluctuations remain closely tied to those of the carrier phase. The model therefore has to reproduce relatively short-memory dynamics, and agreement with DNS-LPT is correspondingly strong. For $St^+ = 23$, the RMS profiles are more closely governed by turbophoresis because gradients in wall-normal turbulence intensity drive inertial particles toward regions of lower turbulent fluctuations near the wall [7]. This makes the intermediate-Stokes-number case a test for emergent phenomena such that the model must reproduce not only the local magnitude of particle fluctuations, but also the way these fluctuations vary across the channel and contribute to wall-normal particle migration. For $St^+ = 23$, the ML model slightly overpredicts the RMS velocity fluctuations, particularly in the streamwise component and in regions where the DNS-LPT profile exhibits sharper wall-normal variation. This may be linked to the finite window length used in the LSTM-based technique. In the intermediate-Stokes-number case, particles have a longer response time and can remain influenced by their previous motion after entering a region of lower turbulence intensity or reduced mean velocity, especially near the wall. If the training window is not long enough to fully represent this residence time and gradual slowing of the particle in that region, the model may retain too much information from the preceding, more energetic part of the trajectory. As a result, the generated particles can carry excess fluctuating energy into near-wall or lower-speed regions, leading to an overprediction of the RMS velocity. The wall-normal component is especially relevant to turbophoresis, since errors in this fluctuation field can alter the balance of transport towards and away from the wall. The general agreement obtained therefore suggests that the model captures the main second-order behaviour needed to represent turbophoretic trends.

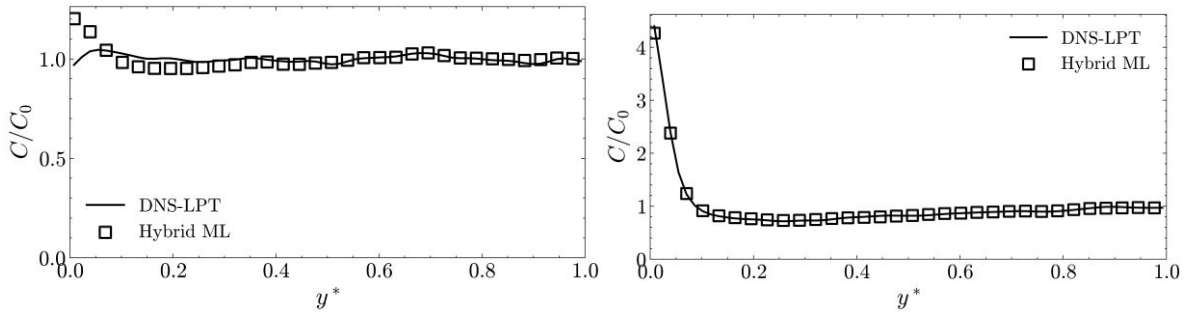

Figure 3: Relative particle concentrations, C/C_0, comparing DNS-LPT against the LSTM hybrid model predictions. Left: $St^+ = 0.03$, right: $St^+ = 23$.

Figure 3 shows the wall-normal particle concentration profiles and provides the most obvious indication of whether turbophoresis has been captured correctly. For $St^+ = 0.03$, the concentration remains close to uniform because the particles are strongly coupled to the turbulent carrier flow and experience little sustained migration relative to the fluid phase. The model reproduces this near-uniform distribution, indicating that it does not generate turbophoretic drift when the particle inertia is very small. For $St^+ = 23$, the concentration profile is more strongly affected by turbophoresis. In this regime, particles do not follow the fastest turbulent fluctuations instantaneously and instead experience a net migration down gradients of turbulence intensity, producing increased near-wall concentrations. The model captures this shift from an almost homogeneous low-Stokes-number distribution to a more wall-accumulated intermediate-Stokes-number distribution. This is a significant result because concentration is an accumulated outcome of many trajectory-level processes, including turbulent dispersion, inertial filtering, wall-normal drift, particle-wall interaction and re-entrainment away from the wall. The close agreement with DNS-LPT therefore suggests that the statistical constraints in the training loss help the generated trajectories preserve the correct long-time turbophoretic balance.

4. Conclusions

A conditional generative LSTM-based hybrid ML model has been developed in order to predict particle-laden turbulent channel flows using DNS-LPT training data. The model was assessed for two

representative particle response regimes, $St^+ = 0.03$ and $St^+ = 23$, corresponding to low and intermediate Stokes number dynamics. For the low-Stokes-number case, the model accurately reproduced the tracer-like particle response, including the mean streamwise velocity, velocity fluctuations, near-uniform concentration profile. For the intermediate-Stokes-number case, the model also captured the main effects of particle inertia, including stronger streamwise persistence, reduced sensitivity to rapid turbulent fluctuations and the development of near-wall accumulation associated with turbophoresis. The concentration profiles were reproduced particularly well, indicating that the model preserves the long-time balance between turbulent dispersion, wall-normal drift, particle-wall interaction and re-entrainment. The main discrepancy was observed in the RMS velocity fluctuations for the intermediate Stokes number, where the ML method slightly overpredicted the DNS-LPT results. This is likely linked to the finite trajectory window length used during training, which may not fully capture the residence time and gradual dynamic adjustment of inertial particles as they move into lower-speed or lower-turbulence regions near the wall. Overall, the results demonstrate that conditional generative LSTM-based hybrid ML models can provide low-cost surrogate predictions of particle-laden turbulent flows while retaining both statistical accuracy and physically realistic trajectory behaviour, although further work should examine longer sequence windows to better resolve the longer memory dynamics of intermediate- and higher-Stokes-number particles.

Acknowledgments
The authors would like to thank Sellafield Ltd. for funding.

References

1. A. Barragán-Montero, U. Javaid, G. Valdés, D. Nguyen, P. Desbordes, B. Macq, S. Willems, D. Vandewinckele, M. Holmström, F. Löfman and S. Michiels (2021). Artificial Intelligence and Machine Learning for Medical Imaging: A Technology Review. Physica Medica, 83:242-256.

2. A. Gupta, A. Anpalagan, L. Guan and A. S. Khwaja (2021). Deep Learning for Object Detection and Scene Perception in Self-Driving Cars: Survey, Challenges, and Open Issues. Array, 10:100057.

3. S. L. Brunton, B. R. Noack and P. Koumoutsakos (2020). Machine Learning for Fluid Mechanics. Annual Review of Fluid Mechanics, 52:477-508.

4. M. Lino, S. Fotiadis, A. A. Bharath and C. D. Cantwell (2023). Current and Emerging Deep-Learning Methods for the Simulation of Fluid Dynamics. Proceedings of the Royal Society A, 479:2275.

5. D. de Oliveira Maionchi, L. Ainstein, F. P. dos Santos and M. B. de Souza Júnior (2022). Computational Fluid Dynamics and Machine Learning as Tools for Optimization of Micromixers Geometry. International Journal of Heat and Mass Transfer, 194:123110.

6. A. Ferrante and S. Elghobashi (2003). On the Physical Mechanisms of Two-Way Coupling in Particle-Laden Isotropic Turbulence. Physics of Fluids, 15:315-329.

7. L. F. Mortimer, D. O. Njobuenwu and M. Fairweather (2019). Near-Wall Dynamics of Inertial Particles in Dilute Turbulent Channel Flows. Physics of Fluids, 31:063302.

8. Z. Wang, D. Xiao, F. Fang, R. Govindan, C. C. Pain and Y. Guo (2018). Model Identification of Reduced Order Fluid Dynamics Systems Using Deep Learning. International Journal for Numerical Methods in Fluids, 86:255-268.

9. P. Jain, A. Choudhury, P. Dutta, K. Kalita and P. Barsocchi (2021). Random Forest Regression-Based Machine Learning Model for Accurate Estimation of Fluid Flow in Curved Pipes. Processes, 9:2095.

10. K. Li, C. Savari, H. A. Sheikh and M. Barigou (2023). A Data-Driven Machine Learning Framework for Modeling of Turbulent Mixing Flows. Physics of Fluids, 35:015150.

11. Z. Yang, K. Li and M. Barigou (2023). Experimentally Trained Hybrid Machine Learning Algorithm for Predicting Turbulent Particle-Laden Flows in Pipes. Physics of Fluids, 35:113309.

12. P. F. Fischer, J. W. Lottes and J. S. Kerkemeier (2008). Nek5000. Available at: http://nek5000.mcs.anl.gov/ accessed 2008.

Resilient groundwater flow modeling in heterogeneous porous media using mixed-form physics-informed neural networks and transfer learning

[1]Xuan-Qi LIU; [1]Kai-Qi LI*; [1]Zhen-Yu YIN;

[1] *Department of Civil and Environmental Engineering, The Hong Kong Polytechnic University, Hung Hom, Kowloon, Hong Kong.*

Abstract

Reliable modeling of groundwater flow in heterogeneous porous media is crucial for the safety and risk assessment of geotechnical and underground infrastructures, where strong subsurface heterogeneity and frequent scenario updates often constrain the effectiveness of conventional numerical solvers and data-driven surrogates. This study develops a mixed-form physics-informed neural networks (PINNs) framework that simultaneously solves for hydraulic head and Darcy velocity, avoiding second-order derivatives and enhancing numerical stability under strongly heterogeneous permeability fields. Spatial heterogeneity is represented via Karhunen–Loève (KL) expansions with controllable correlation lengths, enabling systematic evaluation across statistically consistent permeability realizations. Benchmark tests involving natural gradients and pumping scenarios demonstrate that the mixed-form PINNs can provide more robust predictions under different heterogeneous permeability distributions. To enhance adaptability, transfer learning is incorporated to reuse trained representations across boundary conditions, pumping configurations, and heterogeneous fields, yielding substantial reductions in retraining cost while preserving prediction quality. The results also reveal that transfer directionality (e.g., from more heterogeneous to less heterogeneous fields) is a key factor affecting generalization efficiency. Rather than replacing conventional solvers, the proposed framework offers a flexible, mesh-free alternative for applications requiring frequent model updates or involving intricate subsurface variability, contributing to more resilient and adaptable groundwater modeling in geotechnical practice.

Keywords: Groundwater flow; Physics-informed neural networks; Heterogeneous permeability field; Transfer learning